Complex $nk + m$ Repetitive Controller Applied to Space Vectors: Advantages and Stability Analysis

Rafael C. Neto, *Student Member, IEEE*, Francisco A. S. Neves, *Senior Member, IEEE*, and Helber E. P. de Souza

***Abstract*—Repetitive controllers represent an attractive solution for systems having periodic reference or disturbance signals with high harmonic content. In order to obtain some performance improvements for three-phase plants, as grid-connected converters, complex repetitive controllers were proposed later in literature. In this article, the advantages of complex repetitive control systems over the real ones are analyzed. In addition, sufficient conditions for the input–output stability of complex repetitive control systems and modified complex repetitive control systems are obtained from the small gain theorem. These stability conditions are then used to derive the stability domains for complex repetitive control systems. Further, a relative stability analysis based on the sensitivity function is introduced. An experimental application based on an active power filter is used to exemplify the effectiveness of the proposed stability analysis.**

***Index Terms*—Complex controller, harmonic compensation, repetitive control, stability analysis.**

I. Introduction

THE conventional repetitive controller (RC), as originally proposed [1], is characterized for having a periodic signal generator in its structure. Due to this aspect, and in view of the internal model principle [2], conventional RCs enable the elimination of the system steady-state error for periodic reference signals, even though these signals contain high harmonic content. However, it makes it necessary to store all samples of the error signals during the last fundamental period.

Several real RC-based solutions (i.e., controllers with real input and real output) have been proposed in the past decades. Many of these works approach control schemes with the ability of regulating only a specific family of harmonic components, such as the $4\,k \pm 1$ RC (all odd components) [3], [4], the $6\,k \pm 1$ RC [5], and the $nk \pm m$ RC [6]. When compared to conventional RCs, their main advantage is the smaller number of samples to be stored, which results in a faster response time.

For three-phase systems, RCs are commonly implemented considering decoupled phases or stationary axes. To accomplish this, one can use an RC for each phase quantity (a, b and c) or transform the errors to Clarke's stationary reference-frame and use an RC for each α and β component. However, if the error signal is represented as a space vector, i.e., as a complex variable ($\vec{e} = e_\alpha + je_\beta$), a complex RC becomes an attractive solution [7]. The complex (or vector) approach emerged from proportional-integral controllers in synchronous reference frame (PI-SRF) [8], and some papers were devoted to the modeling and analysis of three-phase systems represented as complex dq-frame systems [9]–[11]. However, the implementation of complex controllers for three-phase systems in stationary reference frame was introduced with the reduced order generalized integrator (ROGI) [12], in 2012. Since then, several studies have approached this methodology, some of the most recent being [13], [14], and [15].

Complex RC structures were first used in a parallel scheme to make the conventional RC achieve a faster transient response [16]. Nonetheless, the output of this strategy, which is the sum of all complex RC structures in parallel, results in a real quantity. Then, this scheme can be applied to separately regulate the α and β components. However, since its input and output signals are real quantities, it does not behave as a complex controller, i.e., it cannot be designed to control a positive-sequence harmonic component without controlling its respective negative-sequence.

In fact, the first RC-based control scheme proposed in the literature that was actually used as complex controller is the one in [7]. These complex RCs can be used to control the harmonic components in the familiy ($nk + m, k \in \mathbb{Z}$) of an error space vector [7], [13], [15]. It is worth noting that, for complex signals, the harmonic spectrum is evaluated so that positive and negative frequencies represent positive- and negative- sequence harmonic components, respectively [15]. Thus, $nk + m > 0$ and $nk + m < 0$ represent positive- and negative-sequence components, respectively. When compared to real RCs (conventional RCs [1] or $nk \pm m$ RCs [4] –[6]), complex RCs provide a faster transient performance and require less memory cells [15].

Although the evaluation of stability of real RCs has been exhaustively approached in the literature [1], [17] –[21], this issue is still an open field for complex RCs. Some researches that propose complex RCs, such as [13] and [15], base their

Manuscript received May 20, 2019; revised September 16, 2019, January 20, 2020, and June 11, 2020; accepted August 13, 2020. Date of publication August 19, 2020; date of current version October 30, 2020. This work was supported in part by the Universidade Federal de Pernambuco, in part by CNPq, and in part by FACEPE. Recommended for publication by Associate Editor Prof. G. Escobar. *(Corresponding author: Francisco Neves.)*

Rafael C. Neto and Francisco A. S. Neves are with the Power Electronics and Drives Research Group (GEPAE), DEE, Universidade Federal de Pernambuco, Recife 50740-530, Brazil (e-mail: rafael.cavalcantineto@ufpe.br; fneves@ufpe.br).

Helber E. P. de Souza is with the Department of Industry, Instituto Federal de Educação, Ciência e Tecnologia de Pernambuco, Pesqueira 50740-540, Brazil (e-mail: helberelias@pesqueira.ifpe.edu.br).

Color versions of one or more of the figures in this article are available online at https://ieeexplore.ieee.org.

Digital Object Identifier 10.1109/TPEL.2020.3017735

stability analysis on the stability domains proposed in [1], even though its applicability is not mathematically proved for complex RCs. Thus, in this article, the input–output stability and relative stability of a complex RC system are mathematically evaluated. Consequently, the present research seeks to come up with stability conditions that can be used as design criteria for these complex RC systems. Besides that, the proposed stability analysis method allows to better evaluate the effect of the parameter a in the proposed complex RC, determining its impact on the system stability domain. Additionally, it makes possible to tune the parameters of the low-pass filter (LPF) that is commonly used in RC-based solutions to improve their stability characteristics. To the best of the authors' knowledge, the article brings the following original contributions:

1) presenting a complex RC based on the primitive repetitive cell proposed in [22], which had been used only for theoretical purpose;
2) presenting a scheme for implementing the complex RC based on the primitive repetitive cell proposed in [22] in real digital signal processors;
3) validating the analysis proposed in [1] for evaluating the input–output stability of complex RCs;
4) establishing the design conditions for ensuring $\mathcal{L}_2$-stability of complex RCs;
5) establishing the magnitude-frequency curve boundary of the LPF used to enlarge the stability domain.

The rest of this article is organized as follows. In Section II, the main differences between real and complex controllers are presented so that the reader can understand the applicability of complex solutions. In Section III, the generic complex RC, its structural characteristics, and its implementation are presented. In Section IV, its input–output stability is evaluated based on the small gain theorem, so that sufficient stability conditions are obtained. Also, a modified complex RC system is introduced to relax the stability condition of the original complex RC system. In Section V, the sensitivity function is used for evaluation of the relative stability in complex RC system. Finally, experimental results considering a three-phase shunt active power filter (APF) are presented in Section VI.

The mathematical notation used in this article is formalized as follows. A continuous-time function $f(t)$ is called bounded in energy, i.e., $f(t)$ belongs to $\mathcal{L}_2$-space ($f(t) \in \mathcal{L}_2$), if $\int_0^\infty |f(t)|^2 dt < \infty$. A discrete-time function $f[i]$ is called bounded in energy, i.e., $f[i]$ belongs to ℓ_2-space ($f[i] \in \ell_2$), if $\sum_{i=0}^{\infty} |f[i]|^2 < \infty$. The set of all proper stable rational transfer functions is denoted by $\mathcal{RH}_\infty$. Considering $G_c(s)$ a single-input–single-output (SISO) continuous-time system, the $\mathcal{H}_\infty$-norm of $G_c(s) \in \mathcal{RH}_\infty$ is defined as $\|G_c\|_{\mathcal{H}_\infty} = sup_{\omega \in \mathbb{R}} |G_c(j\omega)|$. Considering $G_d(z)$ a SISO discrete-time system, the $\mathcal{H}_\infty$-norm of $G_d(z) \in \mathcal{RH}_\infty$ is defined as $\|G_d\|_{\mathcal{H}_\infty} = sup_{\omega_N \in (-\pi,\pi)} |G_d(e^{j\omega_N})|$.

II. Differences Between Real and Complex Controllers

Even though signals and systems in nature are real, some advantages are obtained from the representation of certain phenomena through complex notation. Two application examples of this approach in the field of electrical engineering are the decoupling of instantaneous active and reactive power components, obtained from the instantaneous power theory [23]; and the use of vector control for electric motors [24].

Indeed, if a three-phase power converter is controlled using a synchronous dq reference frame (SRF), then the fundamental-frequency positive-sequence (FFPS) quantities become dc components, making PI controllers separately applied to the d and q axes able to eliminate the steady-state respective errors (PI-SRF). As result, a multiple-input–multiple-output control system is obtained, whose d and q axes are coupled due to the $\alpha\beta$ to dq transformation [9]–[11]. Evaluating this system as a complex vector control system implies considering the d and q (or α and β) signals as the real and imaginary parts of a complex signal (space vector). The resulting complex control system can be evaluated as a SISO system. However, both positive and negative spectra of a complex system frequency response must be evaluated as shown in [9], [10], and also discussed later in this article. Furthermore, it can be shown that adding a complex state feedback to the PI-SRF results in improved system's performance [11].

A vector control system can also be evaluated as a complex system in the stationary $\alpha\beta$ reference frame. This has been done using the so-called reduced-order generalized integrator (ROGI) [12], which is equivalent to a PI-SRF controller transformed to the $\alpha\beta$ reference frame. In fact, since

$$\vec{U}_{dq}(s) = \vec{E}_{dq}(s) \cdot \frac{K_i}{s} \tag{1}$$

$\vec{e}_{dq} = \vec{e}_{\alpha\beta} \cdot e^{-j\omega_0 t}$ and $\vec{u}_{dq} = \vec{u}_{\alpha\beta} \cdot e^{-j\omega_0 t}$, where ω_0 is the frequency of the reference signals to be controlled, equation (1) can be rewritten as

$$\vec{U}_{\alpha\beta}(s + j\omega_0) = \vec{E}_{\alpha\beta}(s + j\omega_0) \cdot \frac{K_i}{s}. \tag{2}$$

In this way, the ROGI is obtained by making the substitution $s \to s - j\omega_0$

$$\frac{\vec{U}_{\alpha\beta}(s)}{\vec{E}_{\alpha\beta}(s)} = \vec{C}_{ROGI}^{(+\omega_0)}(s) = \frac{K_i}{s - j\omega_0} \tag{3}$$

resulting in a controller that has a single complex pole (instead of a pair of complex conjugate poles).

When evaluating the pole and zero diagram of real and complex controllers, it is then observed that while the real controller only allocates real or pairs of complex conjugate poles, the complex controllers may have complex poles without their conjugate ones. An example of this feature is displayed in Fig. 1, where Fig. 1(a) shows the poles and zeros of a second-order generalized integrator (SOGI) while Fig. 1(b) indicates poles and zeros of a ROGI.

From the frequency response of these control structures, considering both positive and negative spectra, it can be seen that the complex solution presents asymmetry with respect to the ordinate axis (Fig. 2).

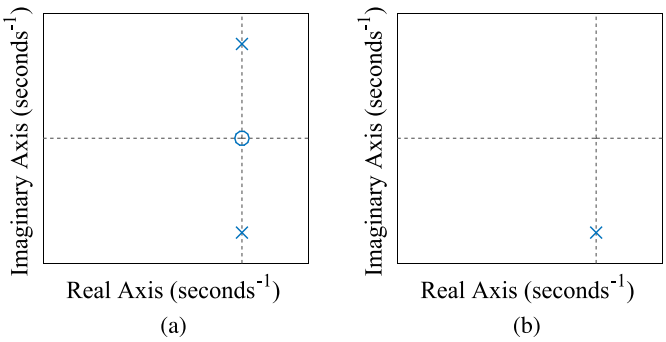

Fig. 1. Poles and zeros diagram for a SOGI and a ROGI. (a) SOGI controller. (b) ROGI controller.

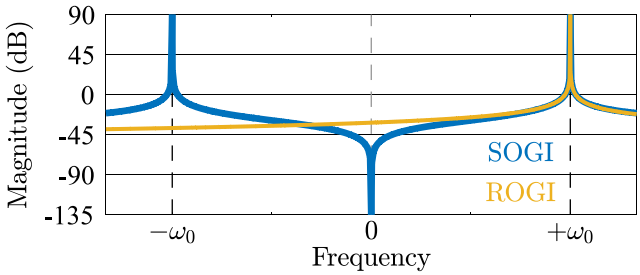

Fig. 2. Frequency response of the SOGI and ROGI controllers.

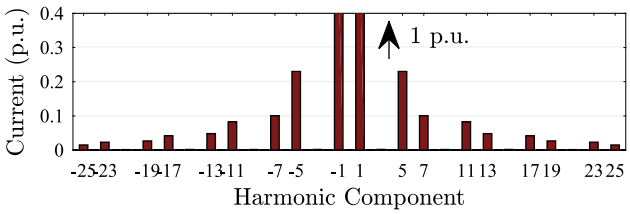

Fig. 3. Harmonic spectrum of the phase current of a three-phase rectifier.

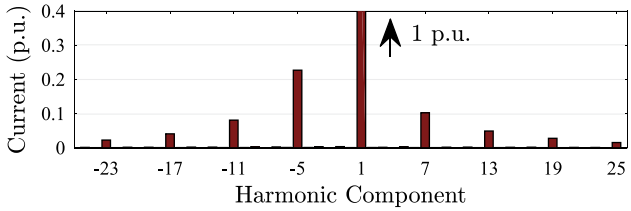

Fig. 4. Harmonic spectrum of the space vector of a three-phase rectifier input current.

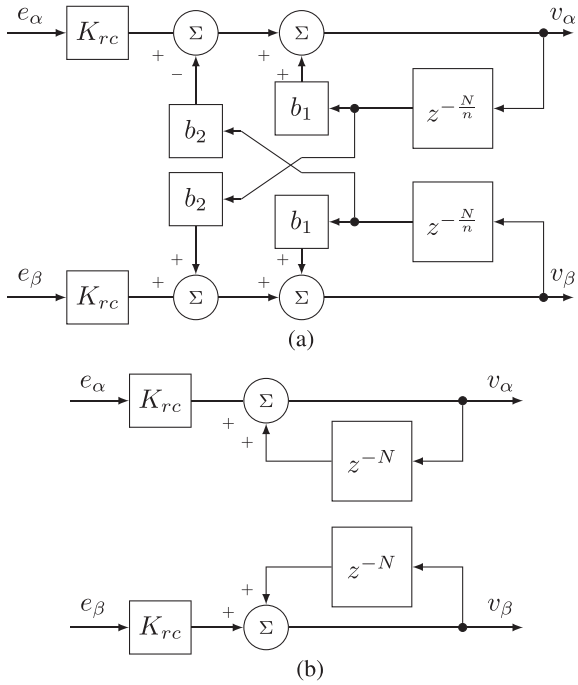

Fig. 5. Block diagrams of complex and real repetitive control structures. Only the complex controller has a coupling between α and β axes. (a) Complex RC proposed in [15]. (b) Real RC proposed in [1].

At first, since the control system references are traditionally real signals, it may seem difficult to notice advantageous applications for the use of complex controllers, but this changes when considering the space vector notation. Indeed, given that a space vector is a complex representation of (real) three-phase signals, its spectral decomposition shows that it represents the positive-sequence components in its positive spectrum, while displaying the negative-sequence harmonic components in its negative spectrum.

In order to understand this concept, a shunt APF used to mitigate the harmonic contamination generated by a three-phase diode rectifier is considered below. Each phase current spectrum of the three-phase diode rectifier has harmonic components in the family ($6\,k \pm 1$, $k \in \mathbb{N}$). Since these signals are real, the harmonic spectrum is symmetrical with respect to the ordinate axis, as shown in Fig. 3. Thus, a real structure can be used to control the APF output currents, which must present high gain for the components of the family ($6\,k \pm 1$, $k \in \mathbb{N}$).

On the other hand, when considering the harmonic spectrum of the space vector obtained from these three-phase currents, it is possible to distinguish positive-sequence harmonic components from negative-sequence harmonic components, as mentioned before. In fact, as shown in Fig. 4, the harmonic spectrum of the space vector obtained from the same currents used for plotting Fig. 3 is asymmetrical. It shows positive-sequence components in the positive spectrum while negative-sequence components are displayed in the negative spectrum. Thus, one can say that this space vector has harmonic content in the family ($6\,k + 1$, $k \in \mathbb{Z}$), i.e., $\{\cdots, -11, -5, +1, +7, +13, \cdots\}$, where the signals "+" and "−" indicate whereas it is a positive- or negative-sequence. As consequence, complex controllers are suitable to control the error space vector of the three-phase control system.

In this scenario, the asymmetric frequency response of the complex controllers is obtained through a coupling between α and β axes, while in real solutions they are decoupled. This feature is shown in Fig. 5 for complex and real repetitive control structures. Exploring the asymmetric frequency response behavior of control schemes has been done since the proposal of PI-SRF, as consequence of the coupling between the α and β axes, performed by the Park transformation.

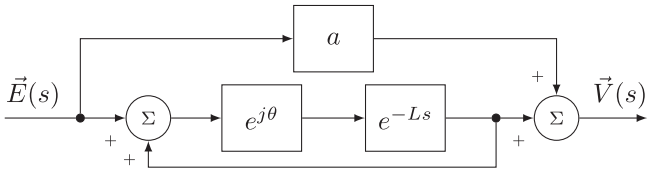

Fig. 6. Complex RC based on the PRC proposed in [22].

III. Fundamentals of Complex RCs

According to the internal model principle [2], a real controller asymptotically tracks a sinusoidal reference signal, with frequency ω_1, if the system's open-loop transfer function (OLTF) has poles allocated at $s = \pm j\omega_1$ and the closed-loop system is stable. This concept can be extended to complex control systems. In fact, a complex controller accurately tracks a positive- (negative-) sequence space vector, with frequency ω_1, if the OLTF has a pole allocated at $s = +j\omega_1$ ($s = -j\omega_1$) and the closed-loop system is stable.

Thus, since complex RCs are characterized by allocating poles at $s = j(nk + m) \cdot \omega_1$ ($k \in \mathbb{Z}$, with constants m and n), they are capable of tracking reference space vectors that contain only harmonic components of the family ($nk + m$, $k \in \mathbb{Z}$). From [7], [13], and [15], its possible to notice that there are several different structures for implementing this control strategy. However, the primitive repetitive cell (PRC) presented in [22] represents the most generic and simplest structure of complex RC.

In [22], this PRC is only approached as an elementary cell for forming more elaborate repetitive controllers. In fact, this structure had only been used for theoretical purposes, aiming to obtain real control schemes. Therefore, in the present article, this PRC is used for the first time as a complex RC.

As shown in Fig. 6, the complex RC based in the PRC proposed in [22] is formed by the following blocks.

1) *A Generic Delay "e^{-Ls}":* By using a periodic signal generator with generic delay $L = T_1/n$, where T_1 represents the period of the fundamental component, the quantity of memory cells demanded by the discrete-time complex RC is $1/n$ of that required by the conventional RC. In addition, it allows to control only the harmonic components in the family (nk, $k \in \mathbb{Z}$).
2) *A Complex Gain "$e^{j\theta}$":* When implementing a complex gain $e^{j\theta}$ along with e^{-Ls}, it shifts the frequency response of the controller. So, for $\theta = 2\pi m/n$, it allows to select a harmonic m so that the complex RC applies high gain in the harmonic components of the family ($nk + m, k \in \mathbb{Z}$), where m is restricted to $0 \leq m \leq (n-1)$.
3) *A Gain "a" in the Second Direct Path:* By selecting a constant value to the parameter a, the controller's structure changes, implying in a different zeros allocation. Therefore, the stability of the closed-loop system where the controller is inserted is affected, as will be mathematically demonstrated in the next section.

Consequently, its transfer function is written as

$$\vec{C}_{RC}^{(nk+m)}(s) = \frac{\vec{V}(s)}{\vec{E}(s)} = a + \frac{e^{j\theta}e^{-Ls}}{1 - e^{j\theta}e^{-Ls}}. \tag{4}$$

It is important to notice that, by assuming $n = 1$ and $\theta = 0$, this complex RC is similar to the conventional RC. Also, for a discrete-time analysis, the generic delay can be implemented as $z^{-N/n}$, where N represents the number of samples per period of the fundamental component. Fig. 7 shows the block diagram of a complex RC system, in which $G(s)$ represents the system's plant and K_{rc} is the controller's gain.

Another relevant point that is worth mentioning is that the controllers proposed in [7], [13], and [15] are particular cases (having different dynamic and stability characteristics) of the complex RC presented here. They can be represented by the proposed complex RC when considering $a = 0.5$, $a = \frac{1+b}{2}$ (b is a parameter of the controller proposed in [13]) and $a = 1$, respectively. Thus, the mathematical approach and the evaluation of the controller's passband described in the following pages can also be extended to [7], [13], and [15].

A. Implementation of the Complex RC

In order to understand how to implement the complex RC in digital signal processors, it is necessary obtain its difference equation from its discrete-time equivalent. Thus, from (4)

$$\vec{C}_{RC}^{(nk+m)}(z) = \frac{\vec{V}(z)}{\vec{E}(z)} = \frac{a + (1-a)e^{j\theta}z^{-N/n}}{1 - e^{j\theta}z^{-N/n}} \tag{5}$$

which can be implemented as

$$\vec{v}[i] = a\vec{e}[i] + (1-a)e^{j\theta}\vec{e}[i - i_d] + e^{j\theta}\vec{v}[i - i_d] \tag{6}$$

for $i_d = N/n$.

Complex mathematical operations, such as $e^{j\theta}$, can be implemented through a matrix system of second order. On the other hand, the space vectors $\vec{v} = v_\alpha + jv_\beta$ and $\vec{e} = e_\alpha + je_\beta$ can be represented as 2×1 matrices. Due to these characteristics, (6) can be rewritten as

$$\begin{bmatrix} v_\alpha[i] \\ v_\beta[i] \end{bmatrix} = a \cdot \begin{bmatrix} e_\alpha[i] \\ e_\beta[i] \end{bmatrix} + (1-a) \cdot \mathbf{B} \cdot \begin{bmatrix} e_\alpha[i - i_d] \\ e_\beta[i - i_d] \end{bmatrix} + \mathbf{B} \cdot \begin{bmatrix} v_\alpha[i - i_d] \\ v_\beta[i - i_d] \end{bmatrix} \tag{7}$$

where

$$\mathbf{B} = \begin{bmatrix} b_1 & -b_2 \\ b_2 & b_1 \end{bmatrix} \tag{8}$$

for $b_1 = \cos(\theta)$ and $b_2 = \sin(\theta)$. Fig. 8 shows the block diagram of the controller implementation using a direct form II structure, in which it is possible to observe that the complex RC has a coupling between the α and β axes.

B. Advantages of Using Complex RCs

In order to understand the main advantages of using complex RCs instead of real RCs, a shunt APF used to mitigate the harmonic contamination generated by a three-phase diode rectifier is again considered, as done in Section II.

By doing so, the three-phase control system can be evaluated as two real control systems (with controllers implemented in α and β axes) or as three real control systems (where the controllers

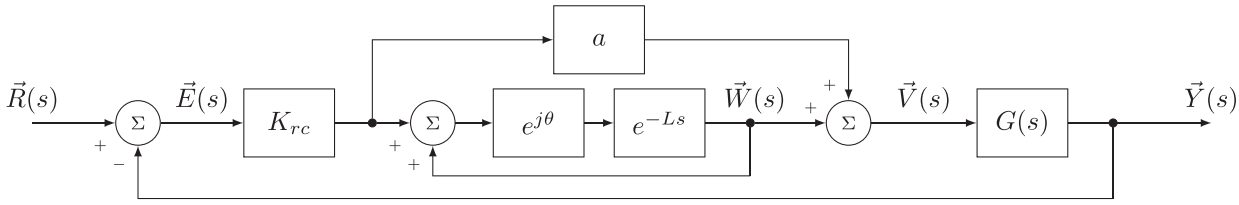

Fig. 7. Block diagram of the proposed complex RC system.

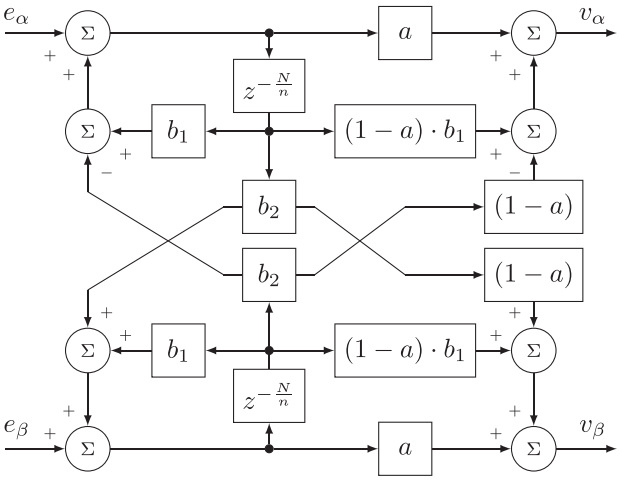

Fig. 8. Implementation of a discrete-time complex RC.

should be used in a, b, and c axes). Since these controllers' references are real signals, their harmonic spectra are symmetrical (Fig. 3), what makes controllers with high gain in the harmonic components of the family ($6\,k \pm 1$, $k \in \mathbb{N}$) the best choice. An example of a suitable controller for the situation is the $nk \pm m$ (real) RC proposed in [22], whose transfer function is

$$C_{RC}^{(nk\pm m)}(z) = K_{rc} \cdot \frac{2\left[1 - z^{-\frac{N}{n}} \cdot \cos\left(2\pi\frac{m}{n}\right)\right]}{1 - z^{-\frac{N}{n}} \cdot 2 \cdot \cos\left(2\pi\frac{m}{n}\right) + z^{-2\frac{N}{n}}}. \quad (9)$$

On the other hand, this same three-phase control system can also be evaluated as a complex control system. By doing so, the reference signal is represented as a space vector, which has high harmonic content in the family ($6\,k + 1$, $k \in \mathbb{Z}$), as can be seen in Fig. 4. As consequence, $nk + m$ (complex) RCs, such as the one evaluated in this section, are suitable to control the error space vector of the three-phase control system.

It is important to note that $nk + m$ RCs result in a sequence-selective solution that controls only the required harmonic components [7]. Besides that, while $nk \pm m$ RCs have several advantages over the conventional RC, complex $nk + m$ RC systems can lead to faster dynamic response than the $nk \pm m$ RC. In order to observe this feature, the real RC represented by (9) can be decomposed into two complex RCs with $a = 1$ (proposed in this article)

$$C_{RC}^{(nk\pm m)}(z) = K_{rc} \cdot \underbrace{\frac{1}{1 - e^{j2\pi\frac{m}{n}} \cdot z^{-\frac{N}{n}}}}_{\vec{C}_{RC}^{(nk+m)}(z) \text{ with } a=1} + K_{rc} \cdot \underbrace{\frac{1}{1 - e^{-j2\pi\frac{m}{n}} \cdot z^{-\frac{N}{n}}}}_{\vec{C}_{RC}^{(nk-m)}(z) \text{ with } a=1}. \quad (10)$$

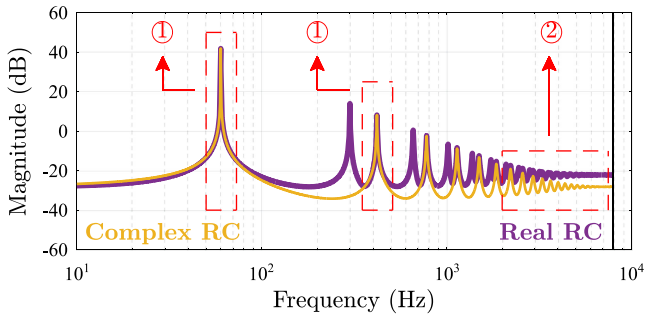

Fig. 9. Magnitude plot of a $6\,k \pm 1$ RC and a $6\,k + 1$ RC, both with same gains and LPFs. ①: The RCs present similar magnitude around low frequency components of the family ($6\,k + 1$, $k \in \mathbb{Z}$). ②: The complex RC has lower magnitude for the high frequency spectrum.

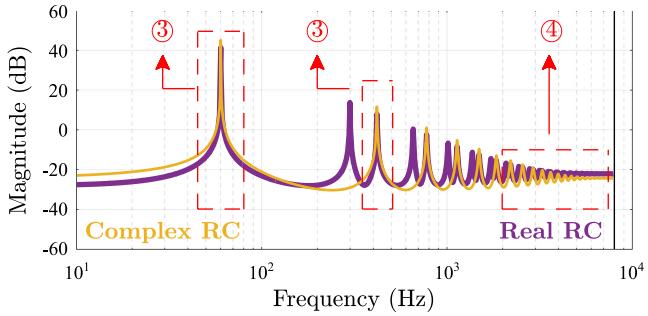

Fig. 10. Magnitude plot of a $6\,k \pm 1$ RC and a $6\,k + 1$ RC, both with equivalent relative stability. ③: The complex RC has higher magnitude around low frequency components of the family ($6\,k + 1$, $k \in \mathbb{Z}$). ④: The RCs present similar magnitude for the high frequency spectrum.

When comparing the bode diagrams (positive spectrum) of the complex RC [only the first right-hand term of (10)] with that of the real RC (the sum of terms), considering same gain and LPF (which is used to increase the relative stability as will be shown in the following section), it is observed that both schemes present similar magnitude response around low frequency harmonic components that belong to family ($6\,k + 1$, $k \in \mathbb{Z}$), as shown in Fig. 9. However, the complex RC has lower magnitude for the high frequency spectrum. Then, if the same gain is used for both schemes, the complex solution will lead to better stability characteristics, without significant changes in the system performance for low frequency harmonic components.

Therefore, if the repetitive gain of the complex RC is increased until both controllers have similar characteristics of relative stability (Fig. 10), the magnitude difference between the high frequency spectrum of the controllers will be lower. Additionally, the magnitude response around the frequency harmonic components that belong to family ($6\,k + 1$, $k \in \mathbb{Z}$) will be higher for the complex solution. As a consequence, the complex

control system will have lower steady-state error, faster transient response, and lower error for small variations in the fundamental frequency. In other words, a complex RC system presents a less restrictive compromise between stability and performance than a real RC system, although, it cannot be used in single-phase control systems.

The Bode diagrams shown in Figs. 9 and 10 are evaluated from a qualitative perspective, i.e., they are used to show that, since the complex RC has better stability properties, its gain can be increased in order to improve the dynamic response. The plots were obtained from a specific example, and the differences between the gains of the complex and real RCs may vary depending on the application, but the abovementioned qualitative characteristics are always true.

Despite the many advantages presented above, this strategy is indicated to three-phase systems with references whose set of positive-sequence harmonic components to be controlled is different from the set of negative-sequence ones. Then, if the harmonic components of positive- and negative-sequence to be controlled are the same, such as in the family ($6\,k \pm 1$, $k \in \mathbb{Z}$) (i.e., $\{\cdots, -7, -5, -1, +1, +5, +7 \cdots\}$), two complex controllers could be used in parallel to accomplish the necessary control tasks, but it would become similar to one of the real RCs previously proposed, such as in (9) and (10). Another limitation to be pointed is that, since single-phase systems do not present asymmetrical harmonic spectrum, the proposed controller's advantages cannot be fully exploited this class of control systems.

In addition, it should be noted that frequency deviations have a high influence in the performance of real and complex RCs. In fact, this happens because, when varying the fundamental frequency of the reference signals, both real and complex RCs no longer will apply high gain in the harmonic components of the reference signals, leading to a large steady-state error as the frequency deviation increases.

IV. Input–Output Stability Analysis of a Complex RC System

At this point the reader must have realized that complex controllers can be represented as two coupled SISO controllers, i.e., as a MIMO controller with two inputs and two outputs. Therefore, since the small gain theorem [25] is valid for MIMO systems, it can be used to evaluate the input–output stability of complex control systems.

Thus, by using the small gain theorem to analyze the error convergence for complex RC systems, it is possible to come up with sufficient conditions under which a bounded input produces a bounded output. The following subsections discuss about these stability conditions.

A. Small Gain Theorem Applied to Complex RC Systems

When considering the complex RC system shown in Fig. 7, its block diagram must be reorganized in order to evaluate its input–output stability through the small gain theorem. Note that $\vec{R}(s)$, $\vec{Y}(s)$, and $\vec{E}(s)$ represent the Laplace transform of the reference $\vec{r}(t)$, output $\vec{y}(t)$, and error $\vec{e}(t)$ space vectors, respectively. In addition, the system's plant $G(s)$ is represented by a proper transfer function and a is a constant gain.

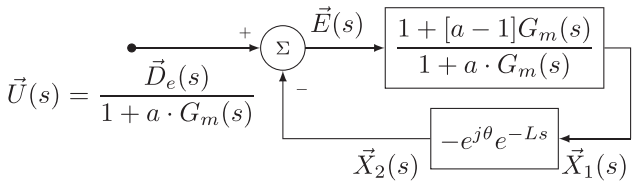

Fig. 11. Block diagram of the complex RC system for the application of the small gain theorem.

From Fig. 7, the following equations are obtained

$$\vec{E}(s) = \vec{R}(s) - \vec{Y}(s) \tag{11}$$

$$\vec{Y}(s) = G(s)\vec{V}(s) + \overline{Y}(s) \tag{12}$$

$$\vec{V}(s) = K_{rc} \cdot a \cdot \vec{E}(s) + \vec{W}(s) \tag{13}$$

$$\vec{W}(s) = e^{j\theta}e^{-Ls}[\vec{W}(s) + K_{rc} \cdot \vec{E}(s)] + \overline{W}(s) \tag{14}$$

in which $\overline{Y}(s)$ and $\overline{W}(s)$ are the Laplace transforms of the initial conditions of $G(s)$ and e^{-Ls}, respectively.

The equations (11)–(13) can still be rewritten as

$$\vec{Y}(s) = \vec{R}(s) - \vec{E}(s) \tag{15}$$

$$\vec{V}(s) = \frac{\vec{Y}(s)}{G(s)} - \frac{\overline{Y}(s)}{G(s)} \tag{16}$$

$$\vec{W}(s) = \vec{V}(s) - K_{rc} \cdot a \cdot \vec{E}(s). \tag{17}$$

Finally, by replacing (15)–(17) in (14), the following equation is obtained

$$\vec{E}(s) = e^{j\theta}e^{-Ls} \cdot \frac{1 + [a-1]G_m(s)}{1 + a \cdot G_m(s)} \cdot \vec{E}(s) + \frac{\vec{D}_e(s)}{1 + a \cdot G_m(s)} \tag{18}$$

where

$$\vec{D}_e(s) = (1 - e^{j\theta}e^{-Ls})[\vec{R}(s) - \overline{Y}(s)] - \overline{W}(s)G(s) \tag{19}$$

$$G_m(s) = K_{rc} \cdot G(s). \tag{20}$$

From (18), it is observed that the complex RC system can be represented by the block diagram shown in Fig. 11. The $\mathcal{L}_p$-stability of this system can be evaluated using the small gain theorem [25].

Since the error space vector of the complex RC system must be bounded in energy in order to obtain zero steady-state error, it is convenient to evaluate the system's input–output stability through its $\mathcal{L}_2$-stability. Therefore, according to the small gain theorem [25], if

i) $[1 + a \cdot G_m(s)]^{-1}\vec{D}_e(s)$ belongs to $\mathcal{L}_2$-space;
ii) $G_1(s) = [1 + a \cdot G_m(s)]^{-1}\{1 + [a-1]G_m(s)\}$ and $G_2(s) = -e^{j\theta}e^{-Ls}$ belong to $\mathcal{RH}_\infty$;
iii) $\|G_1\|_{\mathcal{H}_\infty} \cdot \|G_2\|_{\mathcal{H}_\infty} < 1$;

then, the system's error is bounded in energy, i.e.,

$$\vec{e}(t) = \mathscr{L}^{-1}\{\vec{E}(s)\} \in \mathcal{L}_2 \tag{21}$$

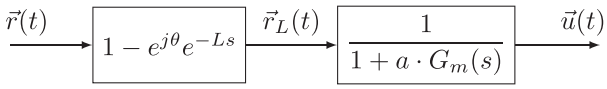

Fig. 12. Block diagram of the input signal of Fig. 11.

TABLE I
$\vec{r}_L(t)$ FOR $\vec{r}(t)=e^{j2\pi t/T_1}$ ($\forall t\geq 0$), CONSIDERING $L=T_1/2$ AND $\theta=\pi$. RESULTS OBTAINED FROM SIMULATION

Signal	$\vec{r}(t)$	$\vec{r}_L(t)$
Real Part: α Axis	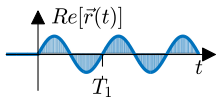	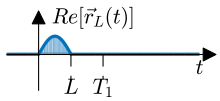
Imaginary Part: β Axis	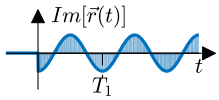	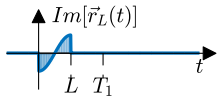

in which $\mathscr{L}^{-1}\{\cdot\}$ represents the inverse Laplace transform.

In view of the fact that the small gain theorem is also applicable to discrete-time control systems [25], these three conditions can also be obtained for discrete-time complex RCs. Therefore, by considering the discretized plant $G(z)$ and (20) rewritten as $G_m(z)=K_{rc}\cdot G(z)$, they become

i) $[1+a\cdot G_m(z)]^{-1}\vec{D}_e(z)$ belongs to ℓ_2-space;
ii) $G_1(z)=[1+a\cdot G_m(z)]^{-1}\{1+[a-1]G_m(z)\}$ and $G_2(z)=-e^{j\theta}z^{-N/n}$ belong to $\mathcal{RH}_\infty$;
iii) $\|G_1\|_{\mathcal{H}_\infty}\cdot\|G_2\|_{\mathcal{H}_\infty}<1$.

The three sufficient conditions are detailed below. In order to facilitate the reader's understanding, all conclusions regarding these conditions are presented in Section IV-A4.

1) Condition (i): When considering Fig. 11, the input signal is defined by

$$\vec{u}(t)=\mathscr{L}^{-1}\{[1+a\cdot G_m(s)]^{-1}\times[(1-e^{j\theta}e^{-Ls})\cdot(\vec{R}(s)-\overline{Y}(s))-\overline{W}(s)G(s)]\}. \tag{22}$$

This space vector can be evaluated for two different hypotheses, i.e., system with zero initial conditions and system with nonzero initial conditions.

For zero initial conditions, (22) can be rewritten as

$$\vec{u}(t)=\mathscr{L}^{-1}\{[1+a\cdot G_m(s)]^{-1}(1-e^{j\theta}e^{-Ls})\vec{R}(s)\} \tag{23}$$

as shown in Fig. 12. So, given that $\vec{r}_L(t)=\mathscr{L}^{-1}\{\vec{R}_L(s)\}$, $\vec{R}_L(s)/\vec{R}(s)$ is equivalent to an operation of the generalized delayed signal cancelation (GDSC) method [26]. This means that if $\vec{r}(t)$ only has harmonic components of the family ($nk+m$, $k\in\mathbb{Z}$), the parameters θ and L (which must be calculated from n and m) can be selected so that the harmonic components of $\vec{r}(t)$ are canceled after L seconds. In other words, $\vec{r}_L(t)$ will be equal to zero for all $t\geq L$ ($L\in\mathbb{R}^+$), i.e., $\vec{r}_L(t)$ will be bounded in energy. A simulation example of this effect is shown in Table I. Finally, by evaluating the second block of Fig. 12, if $[1+a\cdot G_m(s)]^{-1}\in\mathcal{RH}_\infty$, then $\vec{r}_L(t)\in\mathcal{L}_2$ results in $\vec{u}(t)\in\mathcal{L}_2$.

For nonzero initial conditions, $\overline{Y}(s)$ and $\overline{W}(s)$ must be considered. Since these signals represent the initial conditions of the system and they are bounded in energy, by following the same strategy presented for zero initial conditions, $G(s)[1+a\cdot G_m(s)]^{-1}$ must be stable in order for $\vec{u}(t)$ to be bounded in energy.

Since $G(s)[1+a\cdot G_m(s)]^{-1}\in\mathcal{RH}_\infty$ implies $[1+a\cdot G_m(s)]^{-1}\in\mathcal{RH}_\infty$, then $\vec{u}(t)\in\mathcal{L}_2$ if $G(s)[1+a\cdot G_m(s)]^{-1}\in\mathcal{RH}_\infty$ and $\vec{r}(t)$ has only harmonic components canceled by $(1-e^{j\theta}e^{-Ls})$.

When considering the discrete-time complex RC (i.e., e^{-Ls} implemented as $z^{-N/n}$), $\vec{R}_L(z)/\vec{R}(z)$ represents a discrete-time operation of the GDSC method [26]. Thus, for discrete-time complex RCs, $G(z)[1+a\cdot G_m(z)]^{-1}$ must be stable.

2) Condition (ii): Since $G_1(s)$ can be rewritten as

$$G_1(s)=1-\frac{G_m(s)}{1+a\cdot G_m(s)}. \tag{24}$$

Then, if $G_m(s)[1+a\cdot G_m(s)]^{-1}\in\mathcal{RH}_\infty$, the condition $G_1(s)\in\mathcal{RH}_\infty$ is satisfied. As for $G_2(s)$, the following equation is obtained from Fig. 11

$$\vec{x}_2(t)=\mathscr{L}^{-1}\{\vec{X}_2(s)\}=-e^{j\theta}\vec{x}_1(t-L). \tag{25}$$

Equation (25) indicates that $G_2(s)$ delays its input in L seconds, applying a constant gain $-e^{j\theta}$. Since the system is stable and has constant gain for any given frequency, then the condition $G_2(s)\in\mathcal{RH}_\infty$ is always satisfied.

On the other hand, when considering the discrete-time complex RC, (25) can be evaluated as $\vec{x}_2[i]=-e^{j\theta}\vec{x}_1[i-N/n]$. Due to this fact, it is possible to come up with the same conclusions about condition (ii) for discrete-time complex RCs.

3) Condition (iii): By evaluating the $\mathcal{H}_\infty$-norm of $G_2(s)$

$$\|G_2\|_{\mathcal{H}_\infty}=\|-e^{j\theta}e^{-Ls}\|_{\mathcal{H}_\infty}=|-e^{j\theta}|\cdot\|e^{-Ls}\|_{\mathcal{H}_\infty}. \tag{26}$$

Thus, since $|-e^{j\theta}|=1$ (for all θ) and

$$\|e^{-Ls}\|_{\mathcal{H}_\infty}=\sup_{\omega\in\mathbb{R}}|e^{-j\omega L}|=1 \tag{27}$$

the $\mathcal{H}_\infty$-norm of G_2 is always equal to one. So, the condition (iii) is satisfied if

$$\|G_1\|_{\mathcal{H}_\infty}=\left\|\frac{1+[a-1]G_m(s)}{1+a\cdot G_m(s)}\right\|_{\mathcal{H}_\infty}<1. \tag{28}$$

As for discrete-time complex RCs, Equation (27) is replaced by $\|z^{-N/n}\|_{\mathcal{H}_\infty}=1$. Thus, condition (iii) still leads to $\|G_1\|_{\mathcal{H}_\infty}<1$ for discrete-time complex RC systems.

4) Summary of Conditions (i), (ii), and (iii): For continuous-time systems, when the reference space-vector $\vec{r}(t)$ has harmonic components only in the family ($nk+m$, $k\in\mathbb{Z}$) and the complex RC parameters are calculated by

$$L=\frac{T_1}{n}\quad\text{and}\quad\theta=2\pi\frac{m}{n} \tag{29}$$

conditions (i), (ii), and (iii) become

$$\rightarrow\quad G_m(s)[1+a\cdot G_m(s)]^{-1}\in\mathcal{RH}_\infty;\ \text{and} \tag{30}$$

$$\rightarrow\quad\left\|\frac{1+[a-1]G_m(s)}{1+a\cdot G_m(s)}\right\|_{\mathcal{H}_\infty}<1. \tag{31}$$

On the order hand, for discrete-time complex RC systems, these conditions become

$$\rightarrow \quad G_m(z)[1 + a \cdot G_m(z)]^{-1} \in \mathcal{RH}_\infty; \text{ and} \tag{32}$$

$$\rightarrow \quad \left\| \frac{1 + [a-1]G_m(z)}{1 + a \cdot G_m(z)} \right\|_{\mathcal{H}_\infty} < 1. \tag{33}$$

It is possible to note that, if condition (i) holds, then the input–output stability condition for complex RCs becomes equivalent to the one proposed in [1].

It should be noted that any frequency deviation around $1/T_1$ implies that condition (i) will not be satisfied. As a matter of fact, if T_1 is not the fundamental period of the reference space-vector $\vec{r}(t)$, $\vec{r}_L(t)$ will not be bounded in energy, which results in $\vec{e}(t) \notin \mathcal{L}_2$.

Since the input–output stability analysis of both continuous- and discrete-time systems lead to equivalent conditions, the mathematical approach in the following subsections will be conducted using continuous-time notation.

B. Stability Domains for Complex RC Systems

Before presenting the stability domains for complex RC systems, it is important to note that (30) must hold. From the $\mathcal{L}_2$-stability condition shown in (31), it is possible to determine the stability domain of a complex RC system. This domain represents a region of the complex plane in which the Nyquist diagram of the considered plant times the complex RC gain ($G_m(s) = K_{rc} \cdot G(s)$) must be contained in order to satisfy (31). Therefore, this condition may be evaluated by

$$\sup_{\omega \in \mathbb{R}} \left| \frac{1 + a \cdot G_m(j\omega) - G_m(j\omega)}{1 + a \cdot G_m(j\omega)} \right| < 1. \tag{34}$$

In order to simplify notation, consider $X = Re[G_m(j\omega)]$ and $Y = Im[G_m(j\omega)]$. Thus, (34) can be rewritten as (35), as shown at the bottom of this page. Since this last inequality represents the stability boundary condition, the stability domain is obtained by considering the complete transfer function (36), as shown at the bottom of this page, and not only its supremum, which can be handled in order to obtain

$$(1 - 2Re[a])X^2 - 2X + (1 - 2Re[a])Y^2 < 0. \tag{37}$$

Since the imaginary part of a is canceled, a is commonly used as a real constant, as proposed in [1] for conventional RCs. The stability domain of the complex RC system depends on the parameter $a \in \mathbb{R}$, as exemplified in Fig. 13. However, it is worth noting that the three main configurations of complex RC are obtained for $a = 0$, $a = 0.5$, and $a = 1$. This relevance stems from the fact that most real RCs proposed in the literature can be decomposed into complex RCs with these parameters [22].

An example is given as follows to illustrate the input–output stability analysis of the complex RC system through its stability domain. For $a = 0$, the inequality (35) is calculated by

$$Re[G_m(j\omega)]^2 - 2Re[G_m(j\omega)] + Im[G_m(j\omega)]^2 < 0 \tag{38}$$

which represents the region inside the circumference

$$(Re[G_m(j\omega)] - 1)^2 + (Im[G_m(j\omega)])^2 = 1 \tag{39}$$

as shown in Fig. 13(a). On the other hand, for $a = 0.5$, the stability condition is calculated by

$$Re[G_m(j\omega)] > 0 \tag{40}$$

which represents the right half-plane, as shown in Fig. 13(d). Thus, considering these two configurations of complex RCs and the following parameters: reference space-vector $\vec{r}(t) = e^{j2\pi t/T_1}$ ($\forall t \geq 0$), complex RCs with $n = 2$, $m = 1$ and $K_{rc} = 1$, and plant $G(s) = (4\,s + 1)/(s + 2)$; the complex RC system will be $\mathcal{L}_2$-stable for the configuration with $a = 0.5$ [Fig. 14(a)], but not for $a = 0$ [Fig. 15(a)], since the Nyquist diagram of $G_m(s)$ is contained in the shaded region for $a = 0.5$. It should be noted that the closed-loop system would also be stable for those values of a illustrated in Fig. 13(e)–(h).

This example was simulated to allow the error convergence analysis for an $\mathcal{L}_2$-stable system (Fig. 14) and an $\mathcal{L}_2$-unstable system (Fig. 15). As can be seen in Fig. 14(a) and (b), when the Nyquist diagram of $G_m(s)$ is contained in the system's stability domain, both real and imaginary parts of its error space-vector $\vec{e}(t)$ converge to zero. On the other hand, if the Nyquist diagram of $G_m(s)$ is not contained in the system's stability domain [Fig. 15(a)], its error $\vec{e}(t)$ diverges [Fig. 15(b)].

From (32) and (33), it is possible to obtain these same stability domains for discrete-time complex RC systems, however, they are in function of $G_m(e^{j\omega_N})$ (for $\omega_N \in (-\pi, \pi)$). Besides that, the origin of Nyquist complex-plane is not contemplated by any of the stability domains. This happens because the pair ($Re[G_m(j\omega)] = 0, Im[G_m(j\omega)] = 0$) does not satisfy (35), regardless of the selected a. Thus, such as the conventional RC, the complex RC can only be applied to control plants with zero relative degree, i. e., plants with same number of poles and zeros.

C. Modified Complex Repetitive Controller

Most applications of control systems are characterized for having plants with strictly proper transfer functions, i.e., plants with nonzero relative degree. For these systems, the complex RC evaluated in the previous subsections must have its stability conditions relaxed so that its stability domain contemplates the origin of the Nyquist complex-plane.

As done for conventional RCs, the stability conditions of a complex RC can be relaxed by reducing the loop gain of its

$$\sup_{\omega \in \mathbb{R}} \sqrt{\frac{(1 + Re[a] \cdot X - Im[a] \cdot Y - X)^2 + (Re[a] \cdot Y + Im[a] \cdot X - Y)^2}{(1 + Re[a] \cdot X - Im[a] \cdot Y)^2 + (Re[a] \cdot Y + Im[a] \cdot X)^2}} < 1 \tag{35}$$

$$\frac{(1 + Re[a] \cdot X - Im[a] \cdot Y - X)^2 + (Re[a] \cdot Y + Im[a] \cdot X - Y)^2}{(1 + Re[a] \cdot X - Im[a] \cdot Y)^2 + (Re[a] \cdot Y + Im[a] \cdot X)^2} < 1 \tag{36}$$

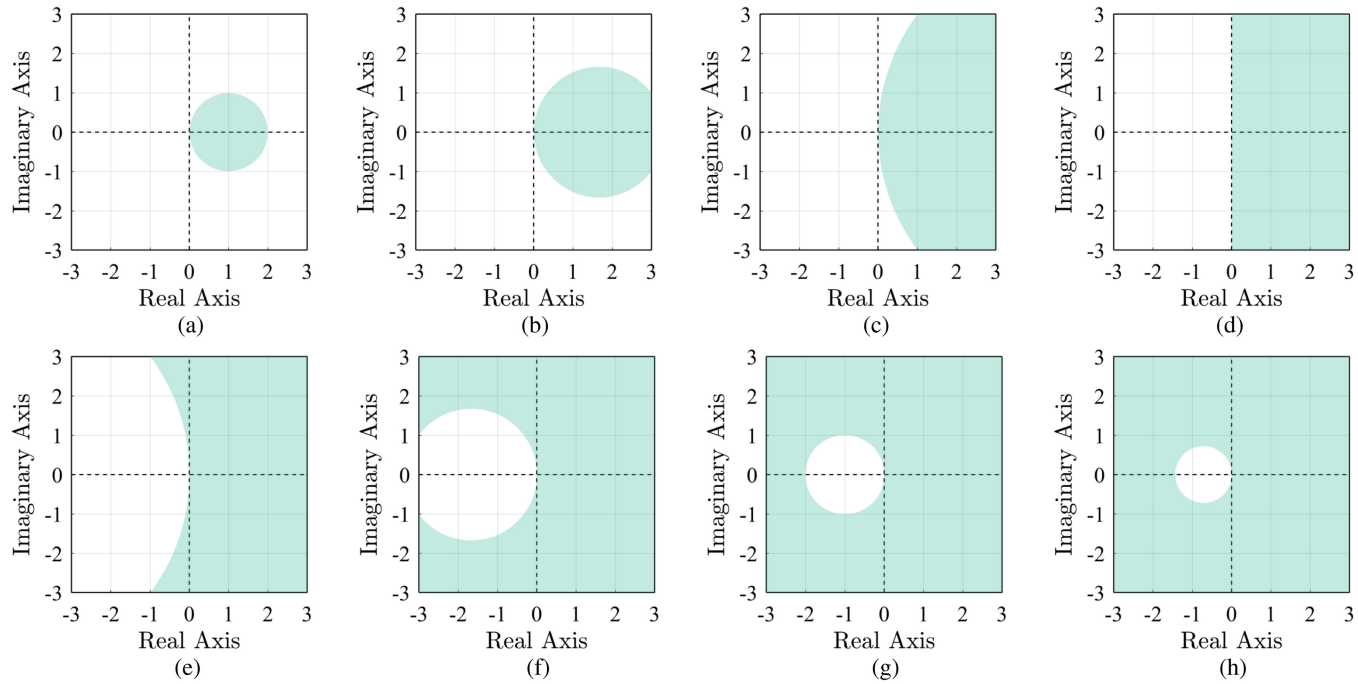

Fig. 13. Stability domains (shaded area) for a complex RC system, which are obtained through the small gain theorem. (a) $a = 0$. (b) $a = 0.2$. (c) $a = 0.4$. (d) $a = 0.5$. (e) $a = 0.6$. (f) $a = 0.8$. (g) $a = 1$. (h) $a = 1.2$.

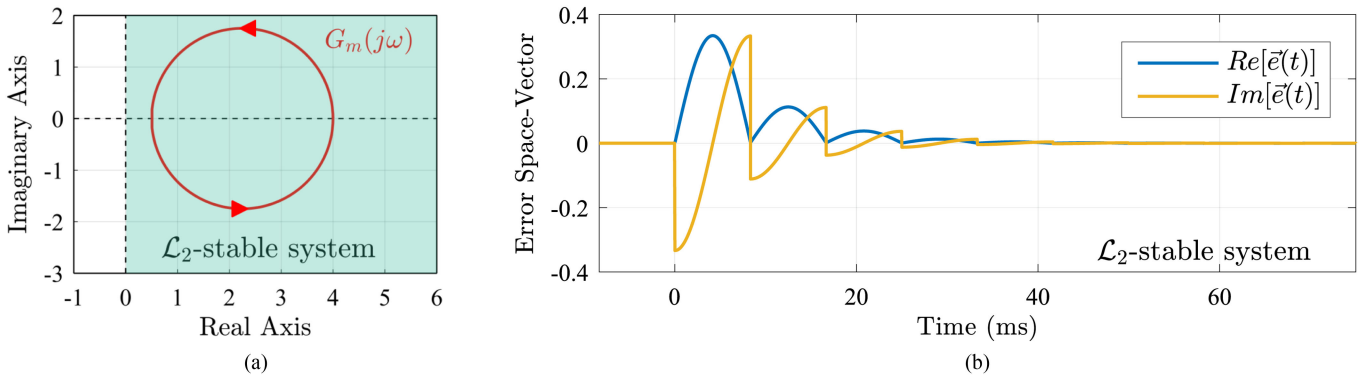

Fig. 14. Error space vector of an $\mathcal{L}_2$-stable complex RC system. Results obtained from simulation. (a) Stability domain of the complex RC system, for $a = 0.5$, and Nyquist diagram of $G_m(s)$. (b) Error space vector of the complex RC system with $a = 0.5$, zero initial conditions, and $G_m(s) = (4s + 1)/(s + 2)$.

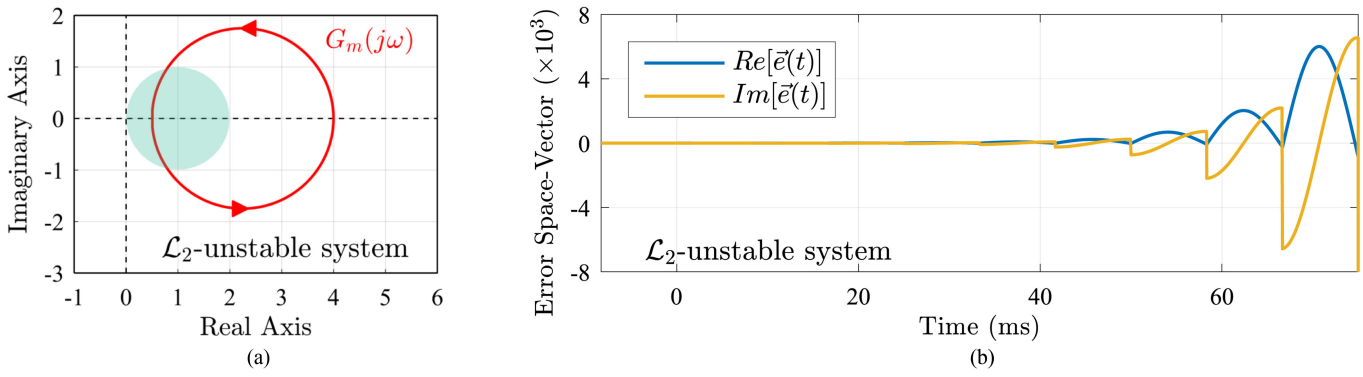

Fig. 15. Error space-vector of an $\mathcal{L}_2$-unstable complex RC system. Results obtained from simulation. (a) Stability domain of the complex RC system, for $a = 0$, and Nyquist diagram of $G_m(s)$. (b) Error space vector of the complex RC system with $a = 0$, zero initial conditions, and $G_m(s) = (4s + 1)/(s + 2)$.

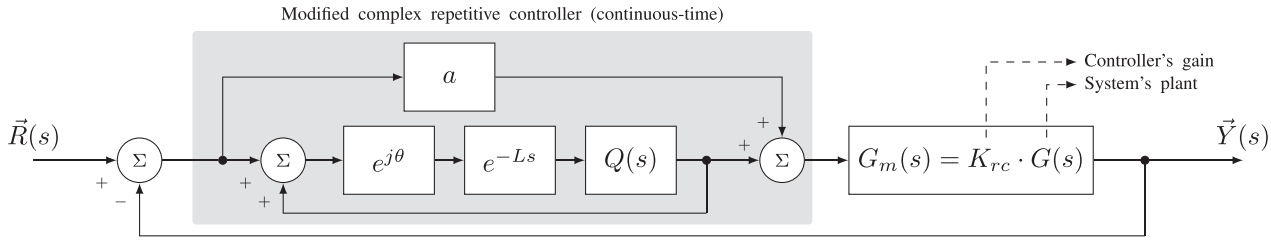

Fig. 16. Block diagram of a modified complex RC system (continuous time).

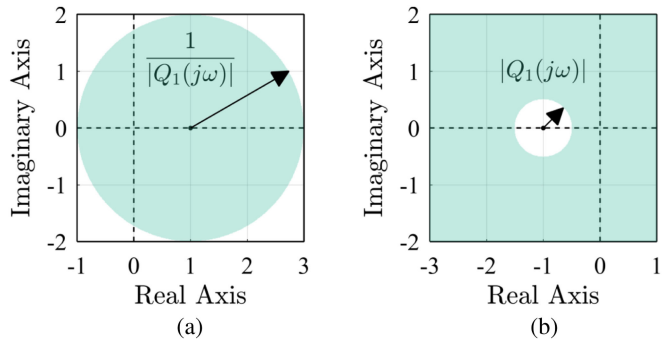

Fig. 17. Stability domains for a modified complex RC system, considering $Q_1(s) = 0.5$. (a) $a = 0$. (b) $a = 1$.

periodic signal generator. This can be done by adding either a constant attenuation or a LPF along with the delay element e^{-Ls} of the complex RC, which is referred to as $Q(s)$ (Fig. 16). Thus, condition (30) is still required, while (31) can be rewritten as

$$\left\| Q(s) \frac{1 + [a-1]G_m(s)}{1 + a \cdot G_m(s)} \right\|_{\mathcal{H}_\infty} < 1. \tag{41}$$

Before presenting the stability domains for modified complex RC systems, it is important to note that (30) must hold. By using the same strategy of the previous subsection, the stability domain of a modified complex RC system with constant $a \in \mathbb{R}$ can be calculated by

$$\begin{aligned} X^2 \cdot f_1(a, |Q(j\omega)|) + Y^2 \cdot f_1(a, |Q(j\omega)|) \\ + X \cdot f_2(a, |Q(j\omega)|) < \left[1 - |Q(j\omega)|^2\right] \end{aligned} \tag{42}$$

in which

$$\begin{aligned} f_1(a, |Q(j\omega)|) = \; & a^2 |Q(j\omega)|^2 - 2a|Q(j\omega)|^2 \\ & - a^2 + |Q(j\omega)|^2 \end{aligned} \tag{43}$$

$$f_2(a, |Q(j\omega)|) = \; 2a|Q(j\omega)|^2 - 2|Q(j\omega)|^2 - 2a. \tag{44}$$

The consequences of using a constant attenuation or an LPF as $Q(s)$ are briefly discussed as follows.

1) $Q_1(s) \rightarrow$ Constant Attenuation: When replacing the delay element e^{-Ls} by $Q_1(s)e^{-Ls}$ (for constant $Q_1(s) < 1$), the lower $Q_1(s)$ the greater is the system's stability domain. This characteristic can be verified by comparing Fig. 13(a) and (g) with Fig. 17(a) and (b). These last two figures show the stability domains for modified complex RC systems ($Q_1(s) = 0.5$) with parameters $a = 0$ and $a = 1$. Both domains of Fig. 17 contemplate the origin of the complex-plane.

It should be noted that the initial condition (i) is no longer satisfied, therefore, even if the system remains stable, $\vec{e}(t) \notin \mathcal{L}_2$. In fact, if (30) and (41) are satisfied for a constant $Q_1(s)$, the error space-vector $\vec{e}(t)$ does not diverge, but still does not converge to zero. This problem can be solved by using $Q(s)$ as an LPF instead of a constant attenuation.

2) $Q_2(s) \rightarrow$ Low-Pass Filter: An LPF can be used to increase the stability domain while keeping the error space-vector bounded in energy. For this, the stability condition shown in (41) must be satisfied for all ω, independently of the LPF characteristics. This fact can be easily understood by considering an LPF with unitary gain in its passband, constant attenuation gain in its stopband, and cutoff frequency $\omega_c = 2\pi f_c$ [Fig. 18(a)], as exemplified in the following.

For all frequencies in which the LPF has a nonunitary gain, the modified complex RC system leads to a nonzero steady-state error, as also observed when $Q_1(s)$ was considered. Then, ideally, the LPF should have an unity-gain passband as large as possible. By doing so, all periodic references whose harmonic components are below the cutoff frequency of the LPF lead to $\vec{e}(t) \in \mathcal{L}_2$. For instance, considering a hypothetical modified complex RC system with $a = 0$ and

$$G_m(s) = \frac{550\, s^2 + 3.459 \cdot 10^7\, s + 2.171 \cdot 10^9}{s^3 + 2628\, s^2 + 5.911 \cdot 10^7\, s + 3.635 \cdot 10^{10}} \tag{45}$$

the maximum acceptable cutoff frequency of the LPF $Q_2(s)$ is around 1 kHz, as shown in Fig. 18. This occurs because the Nyquist diagram of $G_m(j\omega)$ is contained in the stability domain with $|Q_2(s)| = 1$, for all frequencies contemplated by the LPF's passband, i.e., for $|\omega| < \omega_c$ [Fig. 18(a) and (b)]. On the other hand, the maximum acceptable magnitude for the LPF's stopband is bounded, since the gain must be reduced enough for the stability domain to contain the Nyquist diagram of $G_m(j\omega)$ for $|\omega| \geq \omega_c$, as can be seen in Fig. 18(a) and (c).

Besides attenuating high frequency components so that the stability domain is enlarged, LPFs provoke different phase angle displacements on the reference space-vector harmonic components. Because of this behavior, it also modifies the frequencies in which the complex RC allocates its poles. A finite impulse response (FIR) filter represents a viable solution to this problem [27], [28]. This happens due to its linear phase displacement characteristic, which can be adequately compensated by adjusting the delay element of the complex RC [15].

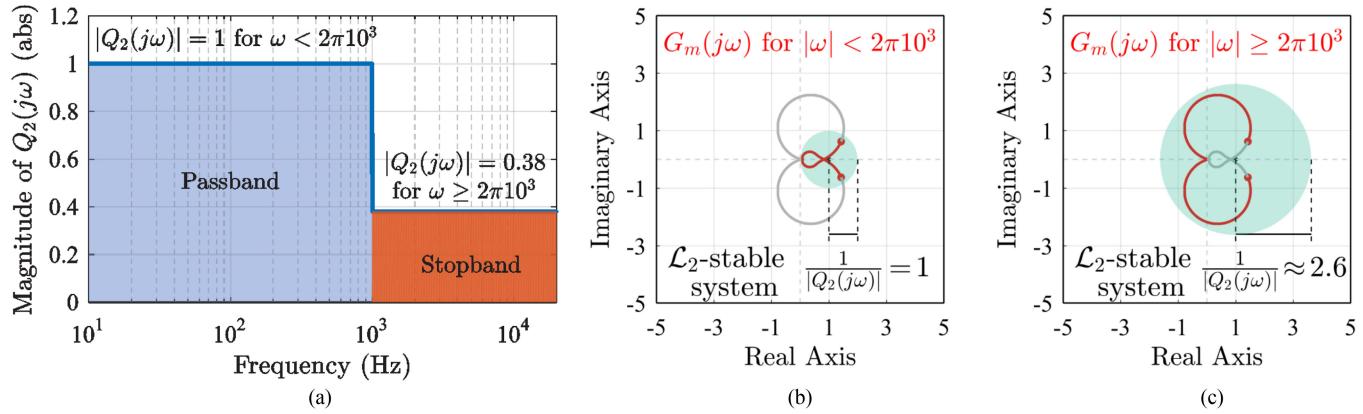

Fig. 18. Stability domains of the modified complex RC system, for $a = 0$, and Nyquist diagram of the $G_m(s)$ presented in (45). (a) Magnitude-frequency response of LPF $Q_2(j\omega)$ with $f_c = 1$ kHz. (b) Stability domain and Nyquist diagram of $G_m(s)$ for $|\omega| < 2\pi 10^3$ rad/s. (c) Stability domain and Nyquist diagram of $G_m(s)$ for $|\omega| \geq 2\pi 10^3$ rad/s.

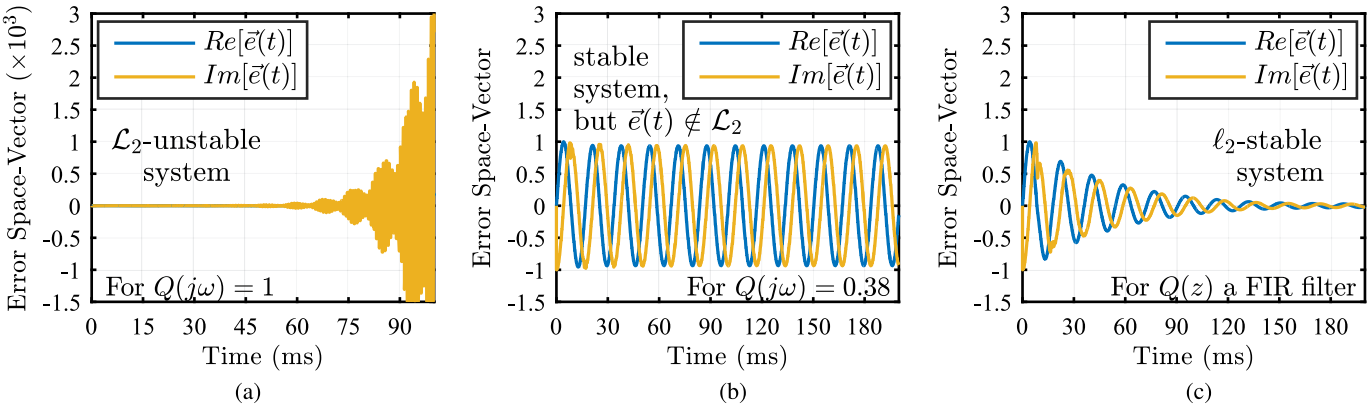

Fig. 19. Error space vector of a modified complex RC system with $a = 0$, zero initial conditions, and $G_m(s)$ presented in (45). Results obtained from simulation. (a) With $Q(j\omega) = 1$, for all $\omega \in \mathbb{R}$. (b) With $Q(j\omega) = 0.38$, for all $\omega \in \mathbb{R}$. (c) For $Q(z)$ being an LPF, with $f_c = 1$ kHz.

An example is given as follows in order to illustrate the $\vec{e}(t)$ convergence. Considering (45) and a discrete-time complex RC with $a = 0$, the following results are obtained.

1) For $Q(j\omega) = 1$ ($\forall \omega \in \mathbb{R}$), the error space-vector $\vec{e}(t)$ diverges [Fig. 19(a)].
2) For $Q(j\omega) = 0.38$ ($\forall \omega \in \mathbb{R}$), the system is not unstable and $\vec{e}(t)$ does not converge to zero [Fig. 19(b)].
3) For $Q(z)$ being the FIR LPF described in (46), the system converges to zero [Fig. 19(a)}, resulting in $\vec{e}(t) \in \mathcal{L}_2$

$$Q(z) = 0.02226 + 0.09105z^{-1} + 0.2335z^{-2} + 0.3064z^{-3} + 0.2335z^{-4} + 0.09105z^{-5} + 0.02226z^{-6}. \quad (46)$$

D. Evaluation of the Passband of Complex RC Through the Stability Domain

The $\mathcal{L}_2$-stability (and ℓ_2-stability) analysis presented in this section can be used to evaluate the passband of the modified complex RC. Therefore, it allows the designer to estimate up to which harmonic component of the family ($nk + m$, $k \in \mathbb{Z}$) the modified complex RC will be able to control. The reader should be aware that the passband of the modified complex RC is evaluated from the cutoff frequency of the LPF used to enlarge the stability domain, so that, it should not be confused with the bandwidth of the closed-loop system.

In order to exemplify this feature, one must initially consider a hypothetical modified complex RC system (discrete-time) with $a = 0$, $K_{rc} = 1$ and

$$G(z) = \frac{0.1741\ z^3 + 0.1201\ z^2 - 0.171\ z - 0.117}{z^3 - 1.663\ z^2 + 1.474\ z - 0.7091}. \quad (47)$$

By doing so, the system's stability domain must contain the Nyquist diagram of $G_m(z) = K_{rc} \cdot G(z)$ for the entire passband of a LPF $Q_2(z)$, which is used to enlarge the stability domain, otherwise the system will be ℓ_2-unstable. Therefore, when considering this modified complex RC system, the cutoff frequency of $Q_2(z)$ (f_{3db}) is limited to 950 Hz, as can be seen in Fig. 20(a). In fact, if this condition holds the system will be stable and its error space vector converges to zero (Fig. 21a). However, if the repetitive gain is increased to $K_{rc} = 1.65$, which can be done to increase the bandwidth of the closed-loop system (decreasing its settling time), it is observed that a range of frequencies below

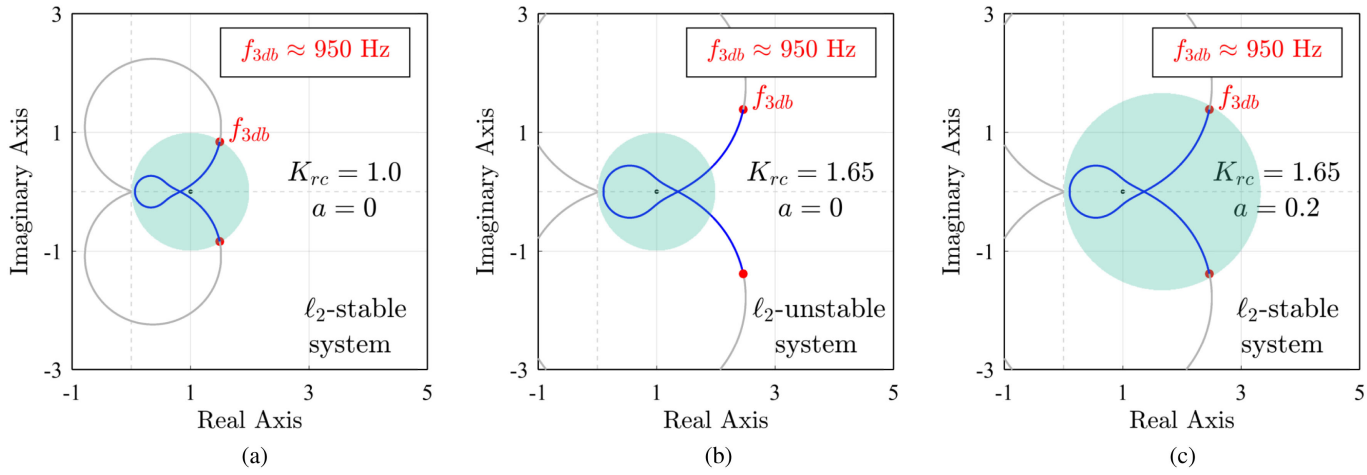

Fig. 20. Stability domain of a modified complex RC system for $|Q_2(je^{\omega_N})| = 1$ and Nyquist diagram of $G_m(z) = K_{rc} \cdot G(z)$, $G(z)$ presented in (47). Plots are used for evaluation of the impact of K_{rc} and a on the ℓ_2-stability of an example system. (a) Plots for $K_{rc} = 1.0$ and $a = 0$. (b) Plots for $K_{rc} = 1.65$ and $a = 0$. (c) Plots for $K_{rc} = 1.65$ and $a = 0.2$.

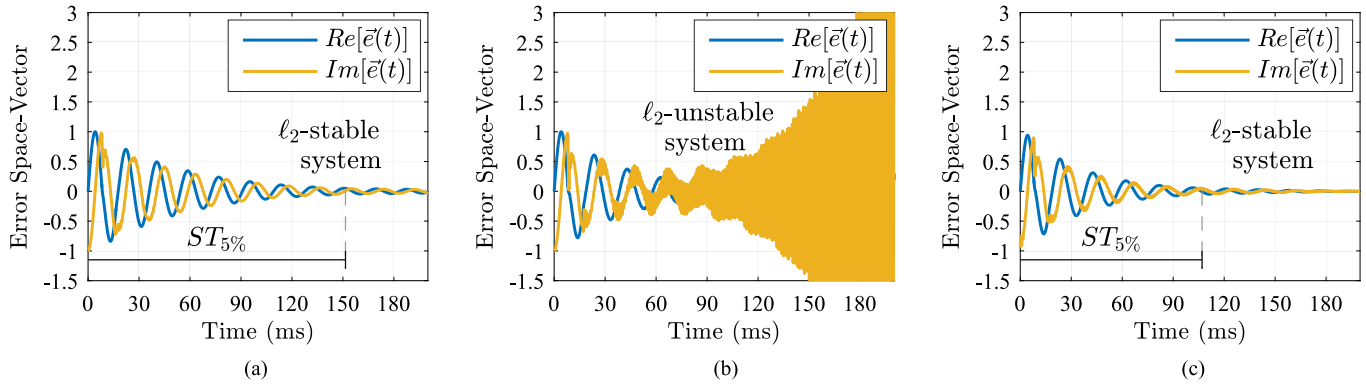

Fig. 21. Error space vector of the modified complex RC systems presented in Fig. 20, for zero initial conditions and FIR LPF $Q_2(z)$ with cutoff frequency $f_{3db} = 950$ Hz. Results obtained from simulation. (a) Results for the system with the stability characteristics shown in Fig. 20(a). (b) Results for the system with the stability characteristics shown in Fig. 20(b). (c) Results for the system with the stability characteristics shown in Fig. 20(c).

f_{3db} are no longer contained in the stability domain [Fig. 20(b)]. As a consequence, the modified complex RC system becomes unstable [Fig. 21(b)].

In this scenario, two solutions arise as follows.

1) The cutoff frequency f_{3db} can be reduced, making the system ℓ_2-stable at the cost of reducing the higher harmonic component of the family $(nk + m,\ k \in \mathbb{Z})$ that will be controlled.
2) The parameter a can be increased until the system's stability domain contemplates the entire passband of the original $Q_2(z)$ [Fig. 20(c)].

For both solutions, the settlement time (5%) is reduced since K_{rc} is increased. This characteristic can be observed when comparing Fig. 21(a) and (c).

Another point to be noted is that, when using an LPF $Q_2(z)$, the passband of the modified complex RC depends on the LPF's cutoff frequency f_{3db}. This happens because for frequencies greater than $f_{3\,dB}$ the magnitude of $Q_2(z)$ is significantly reduced, leading to a considerable steady-state error (as in the example shown in Fig. 19(b) for $Q(j\omega) = 0.38$). Thus, once the parameters a and K_{rc} are selected, the cutoff frequency $f_{3\,dB}$ must be increased to the boundary allowed by the system's stability domain in order to optimize the system performance (Fig. 22).

From the discussion presented in this subsection, one can select the parameters of the modified complex RC (discrete-time) by following the steps.

1) Plot the Nyquist diagram of $G_m(z)$.
2) The parameter a is selected so that the low frequency components of the Nyquist diagram are contained in the stability domain (for $|Q_2(e^{j\omega_N})| = 1$).
3) The repetitive gain K_{rc} is selected by tuning the higher frequency that will naturally be contained in the stability domain (for $|Q_2(e^{j\omega_N})| = 1$). This frequency is used as the cutoff frequency $f_{3\,dB}$ of the $Q_2(z)$.
4) The designer must progressively decrease $|Q_2(e^{j\omega_N})|$ while evaluates the frequency range of the Nyquist diagram of $G_m(z)$ that is contemplated by the obtained stability domain. By doing so, it is possible to determine the magnitude boundary of $Q_2(z)$ for the entire frequency

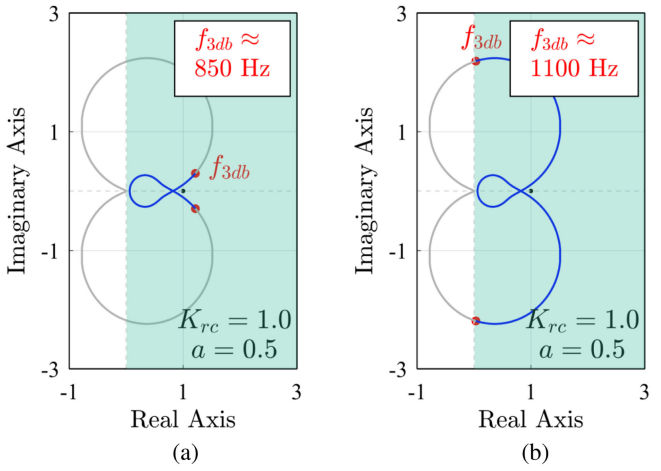

Fig. 22. Stability domain of a modified complex RC system with $a = 0.5$ (for $|Q_2(je^{j\omega_N})| = 1$) and Nyquist diagram of $G_m(z) = K_{rc} \cdot G(z)$, $G(z)$ presented in (47). Plots are used for explain the impact of $f_{3\,dB}$ on the passband of the modified complex RC. (a) Plots for non-optimized $f_{3\,dB}$. (b) Plots for optimized $f_{3\,dB}$.

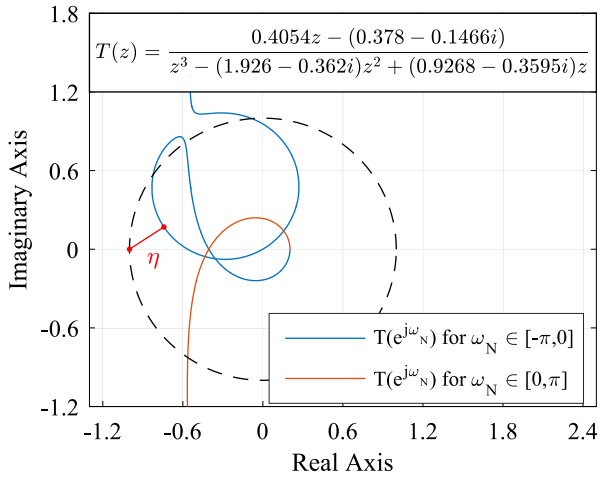

Fig. 23. Nyquist diagram of a minimum phase complex control system. The normalized frequency ω_N is bounded to $[-\pi, \pi]$ because of the Nyquist frequency.

spectrum (as done in Fig. 18). From this analysis, it is possible to define the order of the LPF $Q_2(z)$, which is here referred as M.

5) With M and $f_{3\,dB}$, the FIR filter $Q_2(z)$ is designed.

Finally, the control system designer will have operational values for the parameters a, K_{rc}, and $Q_2(z)$. Nevertheless, the relative stability should be evaluated in order to fine-tune these parameters.

V. Relative Stability Analysis Through Sensitivity Function

In practical situations, even though the designer needs to evaluate the absolute stability of a feedback control system, it is also convenient to analyze its stability degree. In this sense, indicators of relative stability as GM and PM are commonly used for this evaluation.

Back to RC systems, there are some advantages in evaluating the relative stability of a real RC through its sensitivity function, which can also be used in tuning methodologies [29]. For complex RC systems, the sensitivity function still an attractive tool to analyze the relative stability.

For a unitary feedback control system with OLTF $T(s) = C(s)G(s)$, the sensitivity function can be calculated by [30]

$$S_g(s) = \frac{E(s)}{R(s)} = \frac{1}{1 + C(s)G(s)}. \tag{48}$$

Then, let $|S_g(s)|$ be the magnitude of (48) and $1/\eta$ its maximum value, also named sensitivity peak, the inverse of the sensitivity peak (η) can be used as an indicator of relative stability [31]. In fact, since the function

$$D_g(s) = |1 + C(s)G(s)| = |1 + T(s)| \tag{49}$$

represents the distance between the OLTF, $T(s)$, and the critical point $(-1, 0)$ for all frequencies of the Nyquist diagram, the indicator η represents the minimum value of $D_g(s)$.

However, for complex control systems, positive and negative frequencies represent positive- and negative- sequence harmonic components, respectively. Then, both positive and negative frequencies must be considered for the relative stability analysis, in accordance with that presented in [10] and [11]. Fig. 23 shows the indicator η on a Nyquist plot for a complex control system. Thus, it is important to note that all design methods proposed in [29] to real RCs can also be applied to complex RCs.

VI. Experimental Results

In order to obtain experimental results that prove the stability evaluation presented in this article, the output filter of a three-phase shunt APF is used as the plant, as shown in Fig. 24. Thus, the transfer function of the plant in s-domain is

$$G(s) = \frac{\vec{i}_f}{\vec{d}} = \frac{V_{dc}}{L_f s + R_f} \tag{50}$$

where $\vec{d}$ is the space vector obtained from the duty cycles.

As can be seen in Fig. 24, the complex RC is part of the evaluated control system. All digital-time blocks (which are in the blue area of Fig. 24) are implemented in a dSPACE platform, model DS1005 featuring a processor running at 1 GHz. The main characteristics and parameters of the blocks implemented in the dSPACE are briefly described below.

1) The reference generator, which is based in the instantaneous reactive power theory [23], is responsible for producing the APF current references. The block diagram of the implemented reference generator is presented in [32]. This scheme aims to achieve balanced sinusoidal grid currents that are in phase with the voltages at the point of common coupling. Then, it makes possible to compensate the following disturbances: Harmonic distortion, load unbalance, and fundamental-frequency reactive power [32].
2) The feedforward action $\frac{v_1(abc)}{V_{dc}}$ is applied to improve the transient response of the control system. Besides that, it also improves the complex RC ability of rejecting the

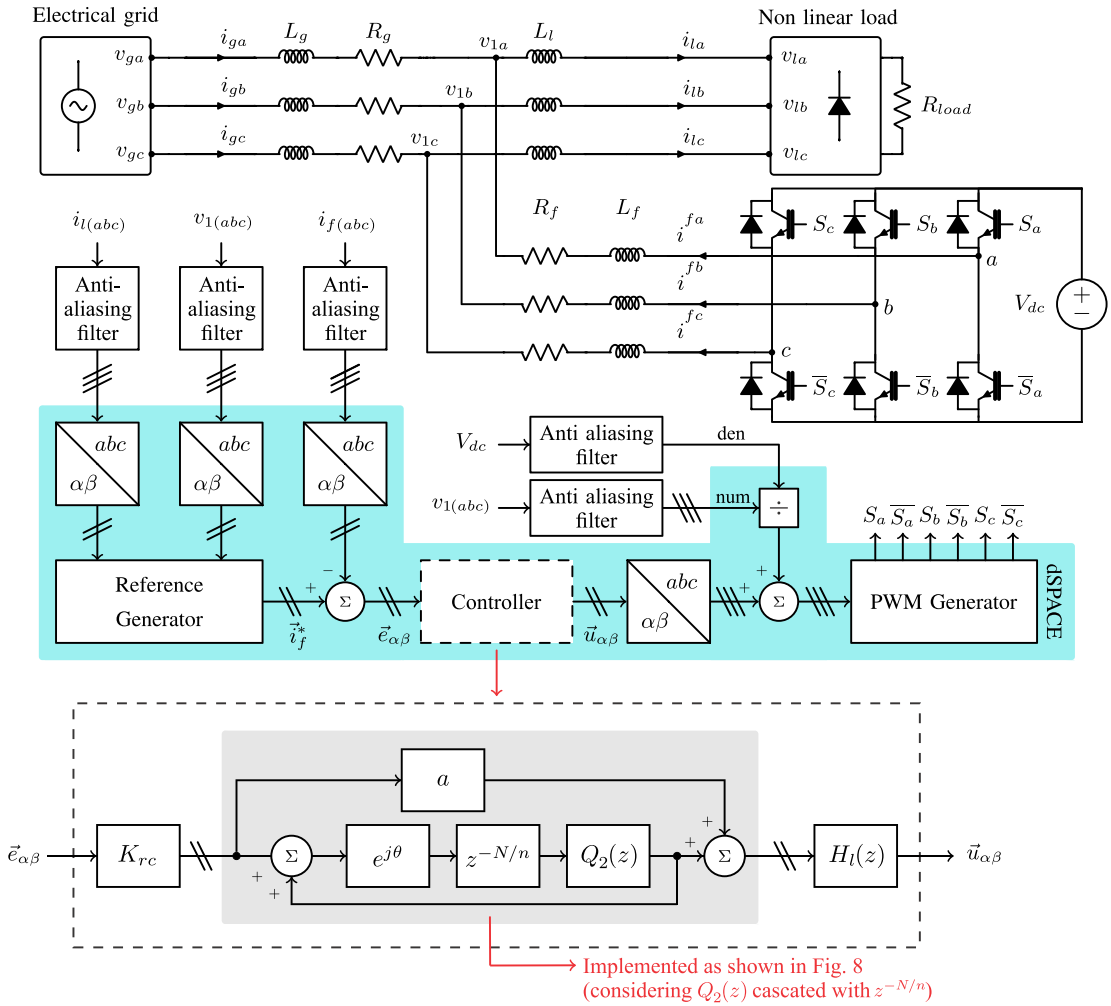

Fig. 24. Complete diagram of the system used for evaluating the proposed complex RC system.

TABLE II
PARAMETERS OF THE EXPERIMENTAL SETUP AND COMPLEX CONTROLLER

Experimental Setup										Complex Controller		
$V_{g(line)}$	L_g	R_g	L_l	L_f	R_f	R_{load}	V_{dc}	f_s *	f_g	K_{rc}	N	a
380 V_{rms}	186.17 μH	31.7 mΩ	1.483 mH	2.563 mH	307.5 mΩ	48.4 Ω	600 V	17.28 kHz	60 Hz	0.060	288	1

*Sampling and switching frequency: $f_s/f_g = N$ must be integer and f_s must be multiple of 32 because of the PLL used for reference generation [33].

impact of voltage disturbances at the point of common coupling ($v_{1(abc)}$).

3) The experimental setup parameters are presented in Table II. Since a three-phase rectifier is used as load, the harmonic components of the load current space vector are in the family ($6k+1$, $k \in \mathbb{Z}$) (as indicated in Fig. 4). Thus, the parameters used for implementing the complex RC are $\theta = 2\pi m/n = \pi/3$ and the delay $z^{-N/n} = z^{-48}$ ($m = 1$ and $n = 6$).
4) The block $H_l(z)$ is a lead compensator used to attenuate the computational delay effect [15].

The dynamic performance of conventional and complex RC structures were compared in [15], being out of the purpose of this article.

For design purpose, the plant is discretized using a ZOH ($G_{zoh}(z)$) and it is increased by a unit time computational delay, modeled as z^{-1} [34]. Since the complex RC error is given in terms of current and its control law in given in terms of duty cycle, its gain was initially used as 0.01. Then, by evaluating the Nyquist diagram of $G_m(z) = 0.01 \cdot z^{-1} \cdot G_{zoh}(z)$, it is possible to note that a modified complex RC is needed in order to $G_m(z)$ be contained in the stability domain, and also, that by using $a > 0.5$ most of $G_m(z)$'s Nyquist diagram remains inside of the stability domain for $|Q_2(e^{j\omega_N})| = 1$. This last point can be seen in Fig. 25, where it is considered the stability domain of complex RC system with $a = 1$.

Thus, the guidelines presented in Section IV-D were used together with design method proposed in [29] for tunning the

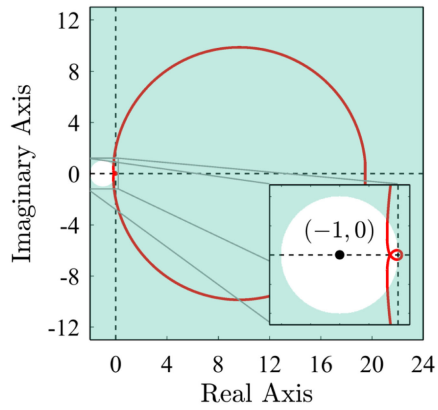

Fig. 25. Stability domain of the complex RC system with $a = 1$ and Nyquist diagram of $G_m(z)$.

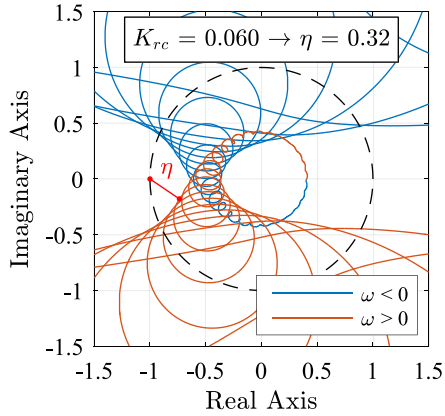

Fig. 26. Nyquist plot of the designed OLTF. Modified complex RC and $H_l(z)$ in a single direct path.

modified complex RC and lead compensator $H_l(z)$ in a single direct path, leading to a sensitivity index $\eta = 0.32$ (Fig. 26). In order to enlarge the stability domain, a symmetrical FIR filter of order $M = 6$ and $f_c = 1.8$ kHz was used as LPF

$$Q_2(z) = 0.0127 + 0.07715z^{-1} + 0.2415z^{-2} + 0.3372z^{-3} + 0.2415z^{-4} + 0.07715z^{-5} + 0.0127z^{-6}. \quad (51)$$

The parameters of the discrete-time complex controller are shown in Table II. Since the control action is directly used as duty cycles of the APF, a small gain K_{rc} was expected.

The new $G_m(z)$ is then defined as $G_{mf}(z) = 0.06 \cdot H_l(z) \cdot z^{-1} \cdot G_{zoh}(z)$. Considering the Nyquist diagram of this transfer function, it is possible to evaluate the magnitude boundary for the LPF $Q_2(z)$, as done for the example illustrated in Fig. 18. In this sense, Fig. 27 proves that the used $Q_2(z)$ satisfies the stability criterion for the designed modified complex RC. As can be seen in Fig. 28, the controller's gain, the lead compensator and the computational delay are all cascaded with the complex RC, becoming part of $G_{mf}(z)$. Thus, the stability domain is not altered by them and the theoretical developments in Section IV are still valid.

Fig. 29 shows the phase-a grid, load, and APF output currents before and after enabling the APF operation. From the analysis

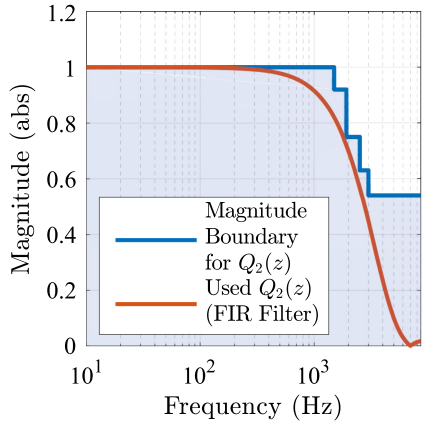

Fig. 27. Magnitude boundary for $Q_2(z)$ and magnitude of the $Q_2(z)$ used to obtain experimental results.

TABLE III
PERFORMANCE COMPARISON BETWEEN THE COMPLEX RC PRESENTED IN THIS ARTICLE AND THE REAL RC PROPOSED IN [22]

Control scheme	Complex RC with $a = 1$	Real RC proposed in [22]	
RC gain	0.060	0.039	0.060
Sensitivity index [31]	0.32	0.32	
0 dB gain crossing frequencies	1.9 kHz	1.9 kHz	ℓ_2-unstable
Settling Time (5%)	$\approx$ 5.5 ms	$\approx$ 8.4 ms	
VTHD of grid currents in steady-state operation [33]	1.66%	2.47%	

of the results, the APF imposed currents caused a reduction in the vector total harmonic distortion (VTHD) of the grid currents [33] from 26.37% to about 1.66%. The VTHD was used here aiming to compute the total harmonic distortion considering both positive and negative frequency spectra. These VTHDs were obtained using the dSPACE platform.

In order to verify the impact of a on the system stability, this parameter is reduced from $a = 1$ to $a = 0.4$ while maintaining the same phase lead of the previous control system. By doing so, the stability domain of the complex RC system is changed as shown in Fig. 30. Since the Nyquist diagram at low frequency (around $\omega = 0$) will not be contained inside the stability domain for any FIR filter $Q_2(z)$ with unit gain in its passband, the complex RC system becomes unstable (as exemplified in Section IV-D). Fig. 31 shows the phase-a grid, load, and APF output currents before and after enabling the APF operation for $a = 0.4$, with the same $H_l(z)$, $Q_2(z)$, and K_{rc} used to obtain Fig. 29.

Fig. 32 shows the reference, compensated, and error currents (for the α axis) during the transient illustrated in Fig. 29. Fig. 33 shows the harmonic spectra of the grid currents during the APF steady-state operation for a complex RC system with $a = 1$ (whose result was presented in Fig. 29). As can be seen in this result, the magnitude of the harmonic components of the grid currents are within the limits defined by the IEEE Standard 519-2014 [35].

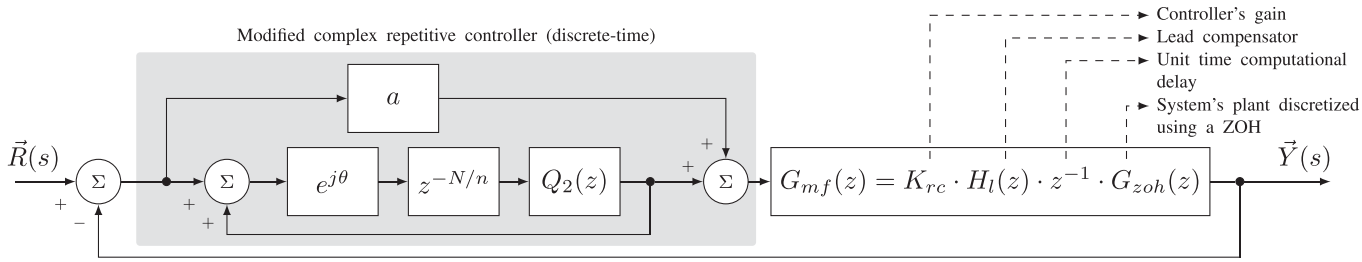

Fig. 28. Simplified block diagram of the modified complex RC system (discrete-time) used for obtaining experimental results.

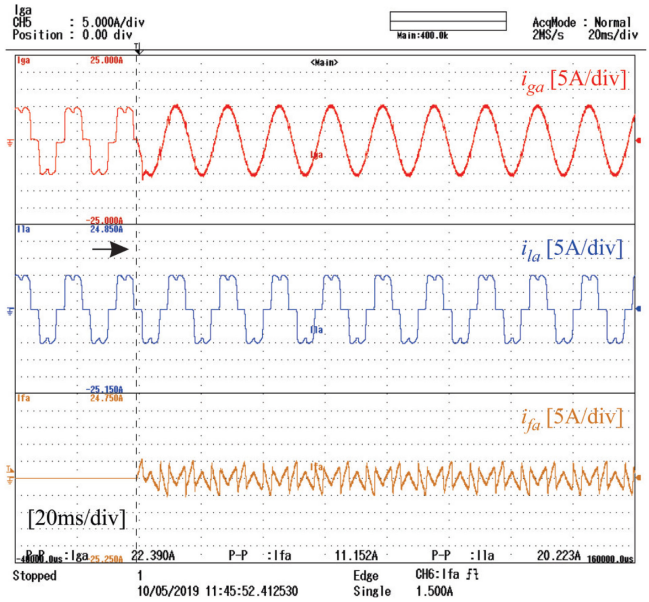

Fig. 29. Phase-a grid, load, and APF output currents before and after enabling the APF operation. Results obtained from experiment for $a = 1$, which indicate system stability.

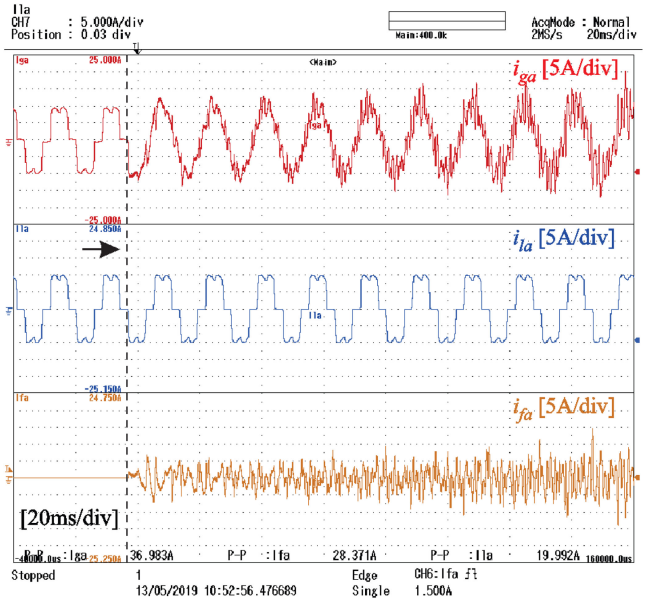

Fig. 31. Phase-a grid, load and APF output currents before and after enabling the APF operation. Results obtained from experiment for $a = 0.4$, which indicate system instability.

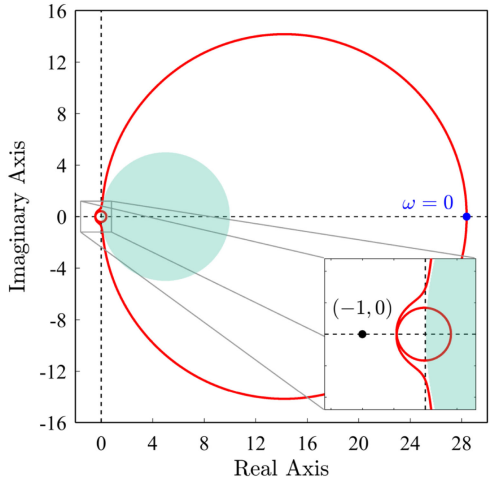

Fig. 30. Stability domain of the complex RC system with $a = 0.4$ and Nyquist diagram of $G_{mf}(z)$.

The operation of the modified complex RC presented in this article was experimentally validated for a load step change (Fig. 34). For this purpose, the resistive load at the dc-side of the three-phase rectifier was varied from $R_{\text{load}} = 48.4\ \Omega$ to $R_{\text{load}} = 32.27\ \Omega$.

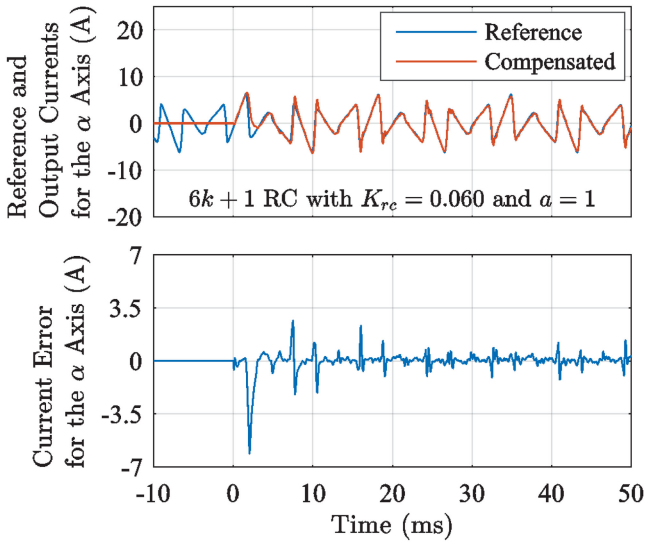

Fig. 32. Reference, compensated and error currents for the α axis. Results obtained from experiment for $a = 1$, using the dSPACE platform.

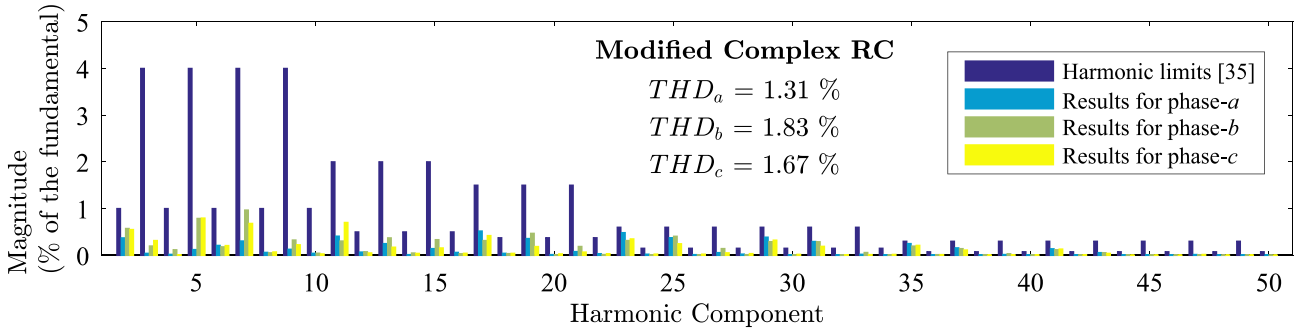

Fig. 33. Harmonic spectra and THD of the grid currents during the APF steady-state operation and harmonic limits according to IEEE Std 519-2014 [35].

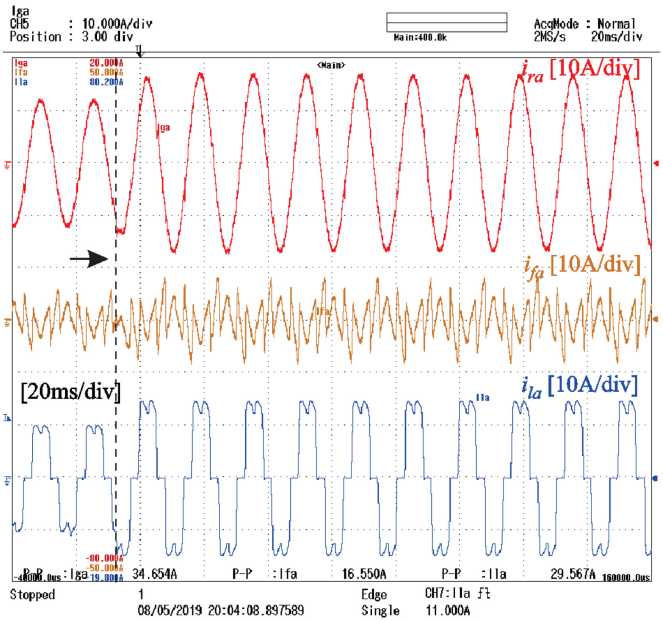

Fig. 34. Phase-a grid, APF output, and load currents for a load step change.

A. Experimental Comparison Between Real and Complex RCs

In order to experimentally verify the advantages of using complex RCs instead of real RCs, the (real) $nk \pm m$ RC proposed in [22] was used to control the prototype described above. This real controller was chosen because it can be decomposed into two complex RCs with $a = 1$ in parallel (one nk), as indicated in (10); therefore, a fair comparison is obtained when using the same $H_l(z)$ and $Q_2(z)$ for both solutions.

Table III shows the settling time (performance indicator of transient operation) and the VTHD of the grid currents space vector (performance indicator of steady-state operation) for the evaluated real and complex RC systems. It should be noted that, when presenting the same sensitivity index and critical 0-dB gain crossing frequency, the complex solution leads to better transient and steady-state characteristics. In fact, as presented in Section III-B, this behavior was already expected since, in order to obtain similar stability characteristics, the complex RC leads to a higher repetitive gain K_{rc}.

As commented in [15], the above validated characteristics can also be explained by the fact that the complex RC has a less restrictive compromise between performance and stability than the real RC. In order to verify it, the authors considered the same repetitive gain K_{rc} for both controllers for a second comparison. Then, for $K_{rc} = 0.060$, the real RC leads to an unstable control system, as indicated in Table III.

VII. Conclusion

This article presents an input–output stability analysis, based on the small gain theorem, for complex RC systems. From this approach, it is possible to come up with stability conditions to complex RC systems and modified complex RC systems. Boundary stability conditions are introduced in order to design the LPF of modified complex RC systems so that stability can be ensured without significantly affecting the control performance. This analysis can be extended to conventional RCs. Also, the use of sensitivity function as indicator of relative stability is extended to complex RCs. Experimental results were used to confirm the validity of the proposed stability analysis. ℓ_2-unstable systems were evaluated through simulations during theoretical analysis.

References

[1] S. Hara, Y. Yamamoto, T. Omata, and M. Nakano, "Repetitive control system: A new type servo system for periodic exogenous signals," *IEEE Trans. Autom. Control*, vol. 33, no. 7, pp. 659–668, Jul. 1988.

[2] B. Francis and W. Wonham, "The internal model principle for linear multivariable regulators," *Appl. Math. Optim.*, vol. 2, no. 2, pp. 170–194, Jun. 1975.

[3] R. Costa-Castello, R. Grino, and E. Fossas, "Odd-harmonic digital repetitive control of a single-phase current active filter," *IEEE Trans. Power Electron.*, vol. 19, no. 4, pp. 1060–1068, Jul. 2004.

[4] K. Zhou, K.-S. Low, D. Wang, F.-L. Luo, B. Zhang, and Y. Wang, "Zero-phase odd-harmonic repetitive controller for a single-phase PWM inverter," *IEEE Trans. Power Electron.*, vol. 21, no. 1, pp. 193–201, Jan. 2006.

[5] G. Escobar, P. G. Hernandez-Briones, P. R. Martinez, M. Hernandez-Gomez, and R. E. Torres-Olguin, "A repetitive-based controller for the compensation of $6\ell \pm 1$ harmonic components," *IEEE Trans. Ind. Electron.*, vol. 55, no. 8, pp. 3150–3158, Aug. 2008.

[6] W. Lu, K. Zhou, D. Wang, and M. Cheng, "A generic digital nk ± m-order harmonic repetitive control scheme for pwm converters," *IEEE Trans. Ind. Electron.*, vol. 61, no. 3, pp. 1516–1527, Mar. 2014.

[7] Z. Luo, M. Su, J. Yang, Y. Sun, X. Hou, and J. M. Guerrero, "A repetitive control scheme aimed at compensating the 6k + 1 harmonics for a three-phase hybrid active filter," *Energies*, vol. 9, no. 10, pp. 787–803, Sep. 2016.

[8] S. Bhattacharya, T. M. Frank, D. M. Divan, and B. Banerjee, "Parallel active filter system implementation and design issues for utility interface of adjustable speed drive systems," in *Proc. 31th IEEE Ind. Appl. Conf. Annu. Meeting*, 1996, vol. 2, pp. 1032–39.

[9] S. Gataric and N. R. Garrigan, "Modeling and design of three-phase systems using complex transfer functions," in *Proc. 30th Annu. IEEE Power Electron. Specialists Conf.*, Jul. 1999, vol. 2, pp. 691–697.
[10] L. Harnefors, "Modeling of three-phase dynamic systems using complex transfer functions and transfer matrices," *IEEE Trans. Ind. Electron.*, vol. 54, no. 4, pp. 2239–2248, Aug. 2007.
[11] J. Shen, S. Schröder, H. Stagge, and R. W. De Doncker, "Precise modeling and analysis of DQ-frame current controller for high power converters with low pulse ratio," in *Proc. IEEE Energy Convers. Congr. Expo.*, pp. 61–68, Sep. 2012.
[12] C. A. Busada, S. Gomez Jorge, A. E. Leon, and J. A. Solsona, "Current controller based on reduced order generalized integrators for distributed generation systems," *IEEE Trans. Ind. Electron.*, vol. 59, no. 7, pp. 2898–2909, Jul. 2012.
[13] R. C. Neto, H. E. P. de Souza, F. A. S. Neves, G. M. S. Azevedo, and Y. N. Batista, "Structures of repetitive controllers based on gdsc with feedforward action," in *Proc. 27th IEEE Int. Symp. Ind. Electron.*, 2018, pp. 533–538.
[14] A. Doria-Cerezo, F. M. Serra, and M. Bodson, "Complex-based controller for a three-phase inverter with an LCL filter connected to unbalanced grids," *IEEE Trans. Power Electron.*, vol. 34, no. 4, pp. 3899–3909, Apr. 2019.
[15] F. J. Zimann *et al.*, "A complex repetitive controller based on the generalized delayed signal cancelation method," *IEEE Trans. Ind. Electron.*, vol. 66, no. 4, pp. 2857–2867, Apr. 2019.
[16] W. Lu, K. Zhou, D. Wang, and M. Cheng, "A general parallel structure repetitive control scheme for multiphase DC–AC PWM converters," *IEEE Trans. Power Electron.*, vol. 28, no. 8, pp. 3980–3987, Aug. 2013.
[17] Z. Shao, Z. Xiang, and H. R. Karimi, "Design of a robust $\mathcal{H}_\infty$ repetitive control system with time-delay," in *Proc. of the 23rd IEEE Int. Symp. Ind. Electron.*, Jun. 2014, pp. 2312–2317.
[18] Y. Ye, Y. Wu, G. Xu, and B. Zhang, "Cyclic repetitive control of CVCF PWM DC-AC converters," *IEEE Trans. Ind. Electron.*, vol. 64, no. 12, pp. 9399–9409, Dec. 2017.
[19] B. Zhang, K. Zhou, and D. Wang, "Multirate repetitive control for PWM DC/AC converters," *IEEE Trans. Ind. Electron.*, vol. 61, no. 6, pp. 2883–2890, Jun. 2014.
[20] F. Califano, A. Macchelli, and C. Melchiorri, "Stability analysis of repetitive control: The port-hamiltonian approach," in *Proc. 56th IEEE Annu. Conf. Decis. Control*, pp. 1894–1899, Dec. 2017.
[21] K. Galkowski, W. Paszke, E. Rogers, S. Xu, J. Lam, and D. H. Owens, "Stability and control of differential linear repetitive processes using an lmi setting," *IEEE Trans. Circuits Syst. II, Analog Digit. Signal Process.*, vol. 50, no. 9, pp. 662–666, Sep. 2003.
[22] R. C. Neto, F. A. S. Neves, H. E. P. de Souza, and C. Rech, "A $nk \pm m$ - order harmonic repetitive control scheme with improved stability characteristics," in *Proc. 27th IEEE Int. Symp. Ind. Electron.*, 2018, pp. 465–470.
[23] H. Akagi, E. Watanabe, and M. Aredes, *Instantaneous Power Theory and Applications to Power Conditioning* (IEEE Press Series on Power Engineering). Hoboken, NJ, USA: Wiley, 2017.
[24] D. Novotny and T. Lipo, *Vector Control and Dynamics of AC Drives* (Monographs in electrical and electronic engineering). Oxford, U.K.: Clarendon, 1996.
[25] C. Desoer, *Feedback Systems: Input–Output Properties*, 1st ed. New York, NY, USA: Academic, 1975.
[26] F. A. S. Neves, M. C. Cavalcanti, H. E. P. de Souza, F. Bradaschia, E. J. Bueno, and M. Rizo, "A generalized delayed signal cancellation method for detecting fundamental-frequency positive-sequence three-phase signals," *IEEE Trans. Power Del.*, vol. 25, no. 3, pp. 1816–1825, Jul. 2010.
[27] G. Escobar, P. Mattavelli, M. Hernandez-Gomez, and P. R. Martinez-Rodriguez, "Filters with linear-phase properties for repetitive feedback," *IEEE Trans. Ind. Electron.*, vol. 61, no. 1, pp. 405–413, Jan. 2014.
[28] Y. R. Teo and A. J. Fleming, "A new repetitive control scheme based on non-causal FIR filters," in *Proc. Amer. Control Conf.*, 2014, pp. 991–996.
[29] R. C. Neto, F. A. S. Neves, H. E. P. de Souza, F. J. Zimann, and A. L. Batschauer, "Design of repetitive controllers through sensitivity function," in *Proc. 27th IEEE Int. Symp. Ind. Electron.*, 2018, pp. 495–501.
[30] K. Ogata, *Modern Control Engineering*, 5th ed. Englewood Cliffs, NJ, USA: Prentice Hall, 2011.
[31] A. G. Yepes, F. D. Freijedo, Ã. Lopez, and J. Doval-Gandoy, "Analysis and design of resonant current controllers for voltage-source converters by means of nyquist diagrams and sensitivity function," *IEEE Trans. Ind. Electron.*, vol. 58, no. 11, pp. 5231–5250, Nov. 2011.
[32] M. A. C. Arcanjo, F. A. S. Neves, G. M. S. Azevedo, and F. Bradaschia, "SVFT-based current control applied to a three-phase active power filter," in *Proc. IEEE 13th Brazilian Power Electron. Conf. 1st Southern Power Electron. Conf.*, 2015, pp. 1–6.
[33] F. A. S. Neves, H. E. P. de Souza, M. C. Cavalcanti, F. Bradaschia, and E. J. Bueno, "Digital filters for fast harmonic sequence component separation of unbalanced and distorted three-phase signals," *IEEE Trans. Ind. Electron.*, vol. 59, no. 10, pp. 3847–3859, Oct. 2012.
[34] S. Buso and P. Mattavelli, *Digital Control in Power Electronics*, 2nd ed. San Rafael, CA, USA: Morgan & Claypool, 2015.
[35] *IEEE Recommended Practice and Requirements for Harmonic Control in Electric Power Systems - Redline*. IEEE Std 519-2014 (Revision of IEEE Std 519-1992) - , 2014.

Rafael C. Neto (Student Member, IEEE) was born in Cabo de Santo Agostinho, Brazil, in 1991. He received B.S. degree in electronic engineering, and the M.Sc. and Ph.D. degrees in electrical engineering from the Universidade Federal de Pernambuco, Recife, Brazil, in 2016, 2018, and 2020, respectively.

He was a Visiting Scholar with the Universidade Federal de Santa Maria, Brazil, in 2016. Since 2020, he has been with the Department of Electrical Engineering, Universidade Federal de Pernambuco, Recife, Brazil. His research interests include power electronics, renewable energy systems, and modeling and digital control techniques of static converters.

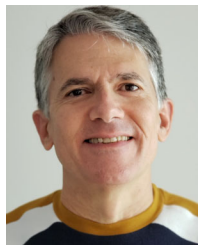

Francisco A. S. Neves (Senior Member, IEEE) was born in Campina Grande, Brazil, in 1963. He received the B.S. and M.Sc. degrees from the Universidade Federal de Pernambuco, Recife, Brazil, in 1984 and 1992, respectively, and the Ph.D. degree from the Universidade Federal de Minas Gerais, Belo Horizonte, Brazil, in 1999, all in electrical engineering.

He was a Visiting Scholar with the Georgia Institute of Technology, Atlanta, GA, USA, in 1999, and at the University of Alcala, Madrid, Spain, from 2008 to 2009. Since 1993, he has been with the Department of Electrical Engineering, Universidade Federal de Pernambuco, Recife, Brazil, where he is a Full Professor. His research interests include power electronics, renewable energy systems, power quality, and grid-connected converters.

Helber E. P. de Souza was born in Cabo de Santo Agostinho, Brazil, in 1983. He received the B.S., M.Sc., and Ph.D. degrees in electrical engineering from the Universidade Federal de Pernambuco, Recife, Brazil, in 2006, 2008, and 2012, respectively.

Since 2009, he has been with the Department of Industry, Instituto Federal de Educação, Ciência e Tecnologia de Pernambuco, Pesqueira, Brazil. He was a Postdoctorate Reseacher with the Universidade Federal de Pernambuco, from 2018 to 2019. His research interests include power quality, grid synchronization methods, and digital control techniques of static converters.